M 2017

U.PORTO
FEUP FACULDADE DE ENGENHARIA
UNIVERSIDADE DO PORTO

POROSITY ANALYSIS ON COMPACTED GRAPHITE IRON

FRANCISCO CABRAL VIANA DA FONSECA

DISSERTAÇÃO DE MESTRADO APRESENTADA
À FACULDADE DE ENGENHARIA DA UNIVERSIDADE DO PORTO EM
MIEMM – MESTRADO INTEGRADO EM ENGENHARIA METALÚRGICA E DE MATERIAIS

Resumo

O objetivo deste trabalho foi investigar o nível de porosidade em amostras de Ferro de Fundido de Grafite Compacta (CGI) com diferentes composições químicas. Foi estudado o grau de grafite nodular, bem como a sua relação com as diferentes quantidades de Mg e Inoculante em cada amostra.

O conceito experimental ligado a este estudo baseou-se na análise de porosidade através do uso de ultrassons, assim como a investigação microestrutural de cada amostra. Foi necessário estabelecer uma relação entre as diferentes composições químicas, as propriedades microestruturais e os dados obtidos a partir da investigação ultrassónica.

A técnica de Color-Etching com base na segregação de silício foi realizada nas amostras de CGI de modo a detalhadamente estudar as suas microestruturas. Foi possível obter dados sobre a cronologia de solidificação.

As superfícies internas da porosidade foram analisadas com o uso da técnica de Microscopia Eletrónica de Varrimento. Verificou-se que a maioria das amostras com alto nível de porosidade continha um elevado grau de grafite nodular.

Foram observadas dendrites de austenite com diferentes morfologias no interior dos poros, indicando que foram formadas em diferentes momentos durante o processo de solidificação.

PALAVRAS CHAVE: Ferro Fundido Compacto, Porosidade, Nodularidade, Processo de Solidificação, Análise por Ultrassons, Ataque Químico, MEV, EDS.

Abstract

The purpose of this work was to investigate the porosity level in samples of Compacted Graphite Iron (CGI) casted with different chemical compositions. The level of graphite nodularity was also studied, as well as its relation with the different amounts of Mg and Inoculant in each sample.

The experimental concept connected to this study was based on the ultrasound investigation of the samples and on their microstructural investigation. There was a need to establish a relationship between the different metallurgical parameters, microstructural properties and data obtained from the ultrasound investigation

An investigation on silicon segregation of the samples of CGI was carried out by applying a selective immersion color etching to study the microstructure. The color etched micrographs of the investigated cast irons provided data about the chronology and mechanism of microstructure formation.

The internal shrinkage-pore surfaces were analyzed by SEM and EDS techniques. It was found that most samples with high porosity level contained a high level of graphite nodularity.

Austenite dendrites with different morphologies were observed inside the pores, indicating they were formed at different times during solidification.

KEYWORDS: Compacted Graphite Iron, Porosity, Graphite Nodularity, Solidification Chronology, Ultrasound Analysis, Color-Etching, SEM, EDS

CONTENTS

INTRODUCTION

This master thesis project was issued on behalf of the Department of Materials and Manufacturing at Jönköping School of Engineering. Supervision and guidance were primarily handled by Professor Attila Diószegi and Professor Carlos Silva Ribeiro, alongside with Professor Vasile-Lucian Diaconu and PhD student Björn Domeij.

Due to its good thermal conductivity, machinability and dumping capacity, lamellar cast iron is most commonly used for the production of engine parts in the automotive industry, although its tensile properties are close to the limit to withstand the elevated combustion pressure [1].

Since there has been an increase in thermal and mechanical loading for modern diesel engines, a change in the type of cast iron used is required, in order to satisfy durability requirements without increasing the size or the weight of the engines [2].

Compacted Graphite iron (CGI) provides at least 70% higher tensile strength and 35% higher elastic modulus than conventional grey cast iron, satisfying durability requirements, with no dimensional stability being compromised [3].

The general understanding of CGI's solidification process is still very limited. In order to predict and prevent casting defects it is necessary to thoroughly study the mechanisms behind the solidification of CGI [4].

The parameters that promote shrinkage porosity in CGI are the fraction of nodular graphite particles in its matrix, the dissolved Hydrogen and Nitrogen content, as well as the number and size of eutectic colonies [5].

- Previous studies have concluded that a higher fraction of nodular graphite particles in CGI, results in higher tendency to macro porosity formation [5];

- Porosity formation increases in CGI by gas precipitation for higher H and N contents in the melt [5];

- A higher number of eutectic colonies leads to a higher level of macro porosity in CGI [5].

After analysing the casted samples produced under standard parameters using an ultrasound equipment, the microstructure presented by CGI is going to be characterized by relating separate regions with and without porosity.
The methods behind this characterization include Optical Microscopy, Scanning Electron Microscope (SEM) and Color Etching. The goal will be to drive a thorough relation between the results and the different variables.

CHAPTER 1

In this chapter, the general literature regarding Compacted Graphite Iron is presented. Topics on the solidification process, the microstructure characteristics and typical defects in this type of cast iron are focused on.

1 COMPACTED GRAPHITE IRON – CGI

1.1 CHARACTERIZATION OF CGI

The compacted graphite iron graphite particles are formed in a vermicular shape, as shown in Figure 1. These individual particles are elongated and randomly oriented, in a similar way as in grey iron, despite being shorter and thicker then these last ones, as well as having rounded edges [6].

While the compacted graphite particles appear in a vermicular shape when viewed in two dimensions, deep-etched scanning electron micrographs (Figure 2) show that the individual particles are connected to other nearest particles within the eutectic cell [7].

Compacted graphite iron invariably includes some nodular (spheroidal) graphite particles. These have an impact on material's properties - as the nodularity increases, the strength and stiffness also increase, while its' castability and thermal conductivity decrease. It is usual to set a limit of 20% nodularity for CGI specifications. [6].

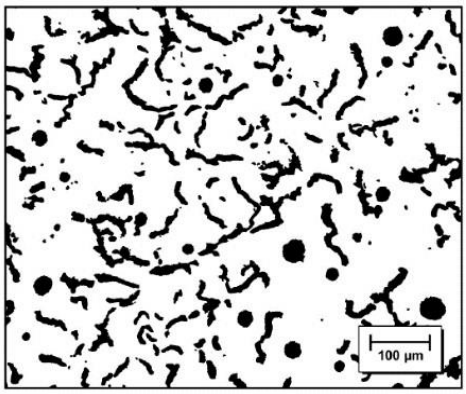

Fig. 1: CGI microstructure presenting 10% nodularity [2]

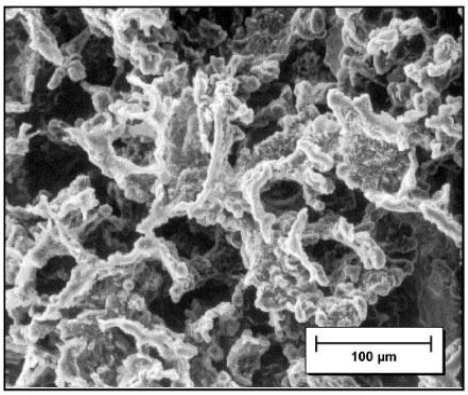

Fig. 2: Deep-etched SEM micrography shows the complex coral-like graphite in three-dimensions [2]

Both the production requirements and the performance conditions of the product influence the microstructure specification adopted. For example, the production of CGI exhaust manifolds is typically specified with up to 50% nodularity. Higher nodularity provides increased strength, which for the case of manifolds, facilitates supporting the exhaust system [7].
In terms of graphite's growth and orientation, it is known that grey iron mainly grows along the A-axis of the graphite lattice, while ductile iron mainly grows along the C-axis, Figure 3 [8].

For the case of CGI, since the graphite has an intermediate shape between grey and ductile iron, its growth behavior is also in between these two types of cast iron. The growth direction of the graphite changes constantly while the transformation takes place, growing both in A and C directions [9].

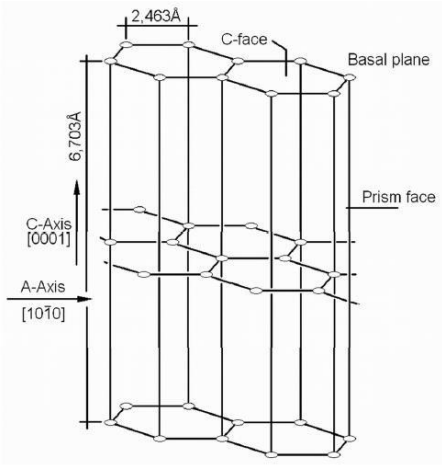

Figure 3: The hexagonally close packed lattice of graphite [8]

The cooling conditions during solidification have also an influence on the graphite morphology – it is expected that high solidification rates result in an increased nodularity [4, 8].

The pearlite content can be varied in order to suit the different required applications for CGI. As an example, exhaust manifolds are generally composed of more than 95% of ferrite, due to its lower thermal conductivity at high temperatures (approximately over 500ºC), which is favorable to prevent higher temperatures caused by high composition of pearlite.

In contrast, cylinder blocks are typically produced with a predominantly pearlitic matrix to maximize the strength and stiffness, while simultaneously providing the adequate hardness to the machining operation [7].

CGI can also be specified with an intermediate ferritic-pearlitic matrix. Within the range of 60-80% pearlite, CGI has approximately the same hardness (BHN 190-225) as a conventional fully pearlitic grey cast iron [7].

1.2 MACHINABILITY

Since in general CGI has approximately 70% higher tensile strength and 35% higher stiffness than grey iron, it is clear that CGI is more difficult to machine than grey iron, although being easier to machine than ductile iron [7].

Through recent optimization processes and tooling developments, CGI milling, drilling and tapping operations can currently provide up to 70% of the grey iron tool life, which previously would be around 50% [7].

The higher strength and stiffness of CGI also results in increased cutting forces. Therefore, CGI machining operations may also require a 20 to 30% higher spindle power and a stronger fixation, than equivalent grey iron operations.

The fact that CGI is easier to machine than ductile iron can influence the replacement between this two types of cast iron in certain applications, as this may lead to better machinability costs, as well as improved castability and mould yield [7].

1.3 THERMAL CONDUCTIVITY

Structural components subjected to thermal stress are highly influenced by the material's thermal conductivity. The higher this one is, the lower the thermal gradients throughout the casting are, and consequently the lower the thermal stress is. On the other hand, the thermal conductivity is greatly influenced by the microstructure of the cast iron, mainly its graphite morphology [10].

It is expected that grey iron has higher thermal conductivity than ductile iron, as shown in Figure 4. On the same note, for higher amounts of graphite, the thermal conductivity is also improved [10].

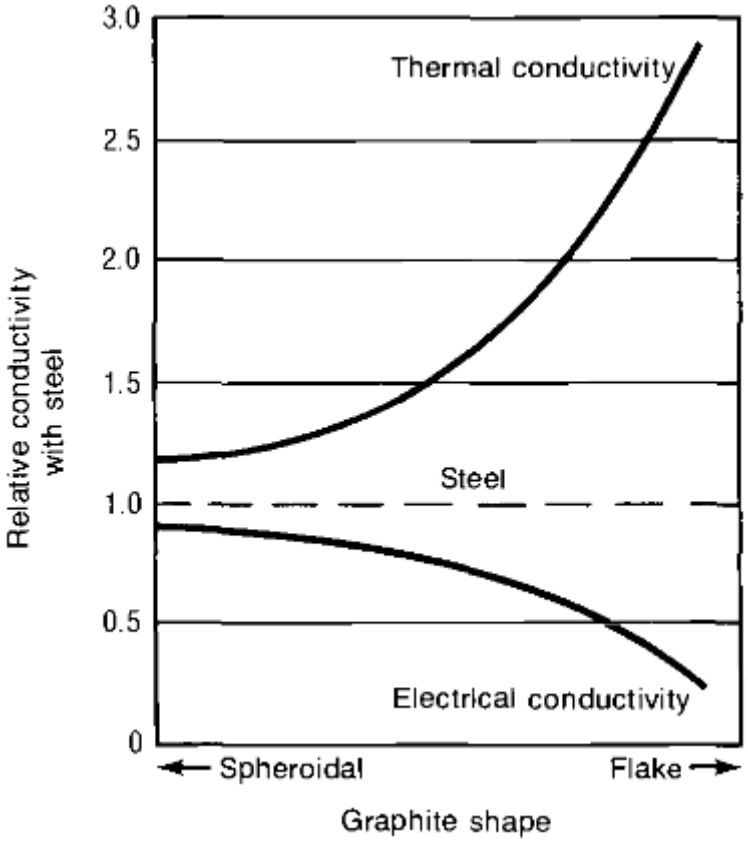

Fig. 4: Influence of graphite shape on the relative thermal and electrical conductivities of Fe-C alloys [10].

The thermal conductivity of Compact Graphite Iron is generally very similar to that of grey cast iron, and substantially higher than that of ductile iron. It can be stated that increased nodularity results in lower thermal conductivity [10].

This is justified by the fact that compacted/vermicular graphite is interconnected, as flake graphite is. Also, increasing the carbon equivalent results in higher thermal conductivity for CGI. [10].

1.4 TENSILE PROPERTIES AND HARDNESS

Compacted graphite irons exhibit linear elasticity for both pearlitic and ferritic matrices (Figure 5) [10].

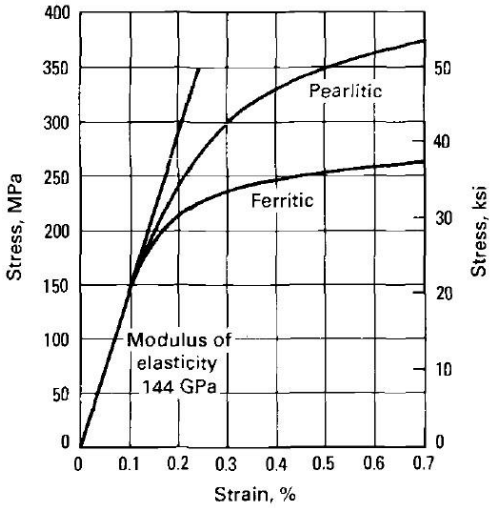

Fig. 5: Typical stress-strain curves for CG irons. The pearlitic iron presents a tensile strength of 410 MPa and an elongation of 1%. The ferritic iron shows a tensile strength of 320 MPa and an elongation of 3.5% [10].

The ratio between yield strength and tensile strength for CGI ranges from 0.72 to 0.82, which is higher than that for ductile iron of the same microstructure. This makes it possible to achieve a higher loading capacity [10].

As hardness increases, tensile strength increases although the elongation decreases. This is caused by the higher pearlite/ferrite ratio (Figure 6) [10].

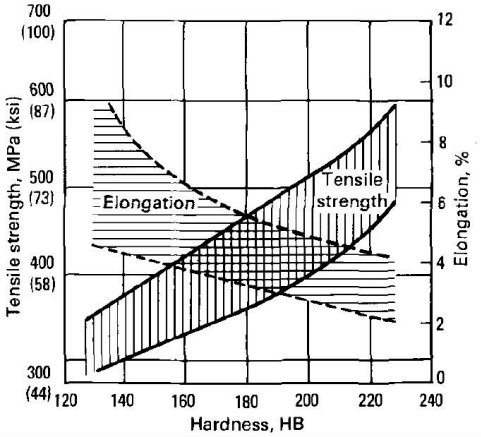

Fig. 6: Correlation between hardness, tensile strength, and elongation in CG irons [10].

The ratio between tensile strength and Brinell hardness is slightly higher for CGI than it is for grey iron. In general, CG iron has lower hardness than a grey iron of equivalent strength, because of the higher amount of ferrite in the CGI's structure [10].

2 PROCESS CONTROL OF CGI

The stable range for the relationship between the % nodularity and the % Mg for the production of CGI is very narrow, which is the main reason why it is very hard to guarantee a risk-free CGI product. [3].

The stable CGI plateau generally covers a range of approximately 0.008% Mg, as shown in Figure 7, although its actual size and location is different for each product [3].

Since the active magnesium fades at a rate of approximately 0.001% every five minutes, its initial amount should be carefully controlled, in order to prevent the abrupt CGI-to-grey iron transition. Before the metal is fully poured, it needs to be assured that the formation of flake-type graphite does not occur [3].

Likewise, the formation of nodular graphite in the faster-cooling thin sections must be avoided, so the starting point cannot be too close to the right side of the plateau [3].

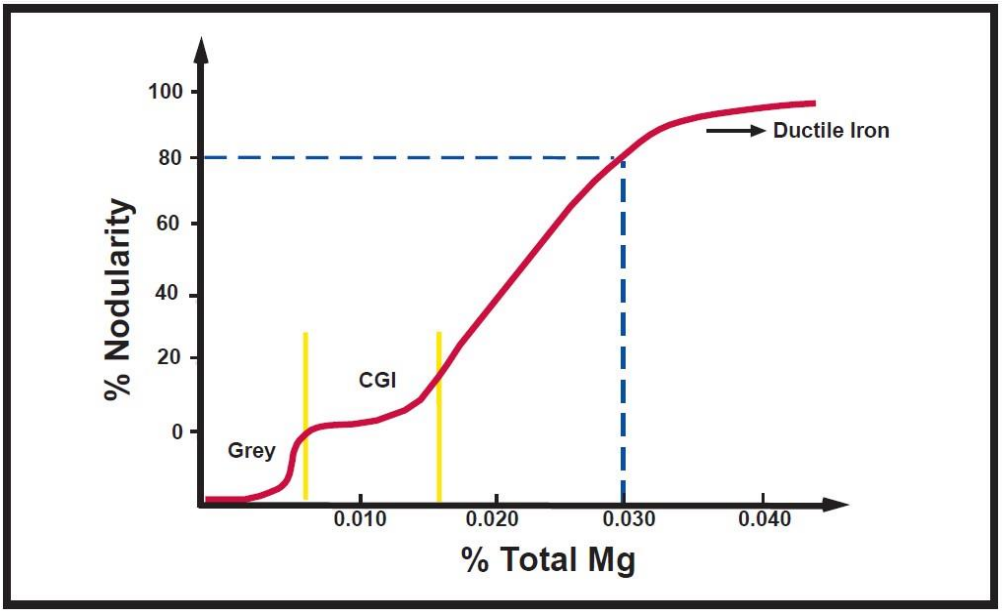

Figure 7: The stable CGI plateau exists over a range of approximately 0.008% magnesium and is separated from grey iron by an abrupt transition [3]

The stable CGI plateau is not considered stationary, which means that if the active oxygen and/or sulfur contents are high, the active magnesium will be consumed and the entire plateau shifted towards higher total magnesium values. On the other hand, if the oxygen or sulfur levels are relatively low, the CGI plateau will shift towards the left [3].

Figure 8 illustrates the influence of magnesium in CGI. It shows that a 25 mm diameter test bar of a structure with flake-shaped particles can be converted into a fully compacted microstructure, with the addition of only 10 grams of magnesium in a one tone ladle.
The flake-shaped microstructure provides a tensile strength of 300 MPa while the tensile strength of the fully compacted microstructure is 450 MPa [3].

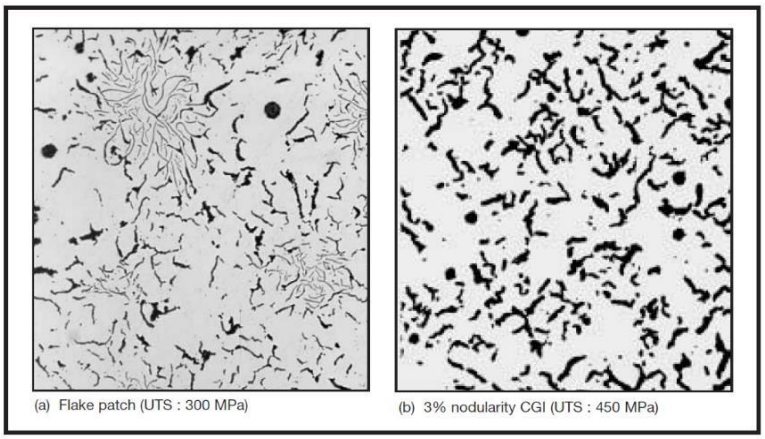

Figure 8: An addition of 0.001% active magnesium is sufficient to convert a flake-patch microstructure into a high quality CGI microstructure [3].

CGI is also very sensitive to the addition of inoculant, with higher inoculation levels favoring the formation of nodular graphite. Processing factors such as furnace superheat, holding time, charge composition and type and amount of inoculant have an influence on whether or not a CGI is obtained. [3].

The sensitivity to inoculation is illustrated in Figure 9, which shows that the addition of 0,08% of inoculant can change the nodularity from 3% to 21% in a 25 mm diameter test bar [3].

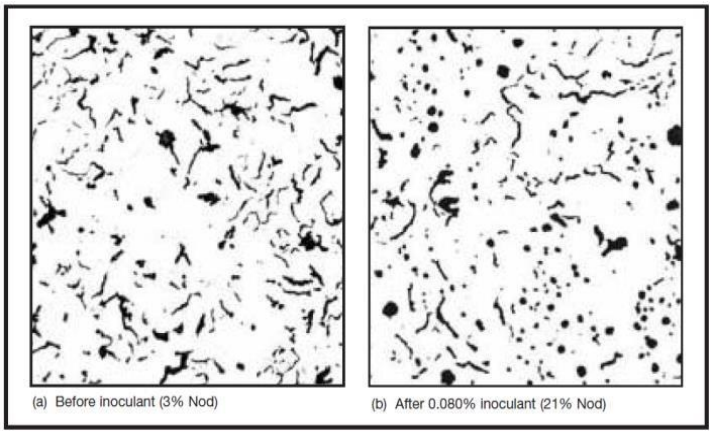

Figure 9: An addition of 0.08% post-inoculant can cause the CGI nodularity to increase from 3% to 21% in a 25 mm diameter test bar [3]

2.1 PRODUCTION CONSIDERATIONS

When it comes to the production of CGI, the range of acceptable carbon and silicon contents for the production of CGI is rather wide, as it is shown in Figure 10 [10].

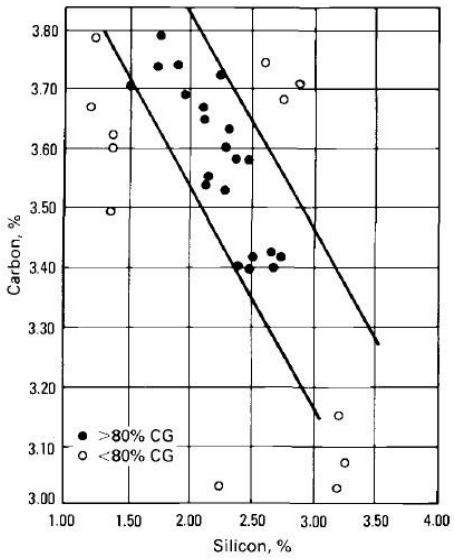

Figure 10 - Optimum range for carbon and silicon contents for CG iron production [10]

In the production of CGI, the chemical composition of other alloying elements must also be taken into consideration.

The manganese content can vary between 0,1 and 0,6%, depending on whether a ferritic or a pearlitic structure is desired. Phosphorus content should be kept below 0,06% in order to obtain maximum ductility from the matrix. The initial sulfur level should be below 0,02%.[10].

The ladle where the melt is charged into needs to be preheated, usually by gas flame, at a temperature of up to 1520 to 1530ºC, before the melt is poured from the furnace [1].

The next step consists in the addition of active elements, FeSiMg and rare earth metals into the ladle. These act as nodularizers and help in the oxygen and sulfur removal. The alloying elements are normally covered by a buffer, called alloying pocket, which delays the reaction between the hot metal and these elements until all the metal is charged. This helps to control the fading effect of magnesium and prevents wasting expensive rare earth metals [1].

CGI is sensible to both magnesium and inoculant, which means that CGI is stable not on a simple magnesium plateau, but as it is illustrated in Figure 11. The production of reliable CGI therefore requires simultaneous control of the magnesium and inoculant from the start until the end of the process, in order for it to stay within the microstructure specification [3].

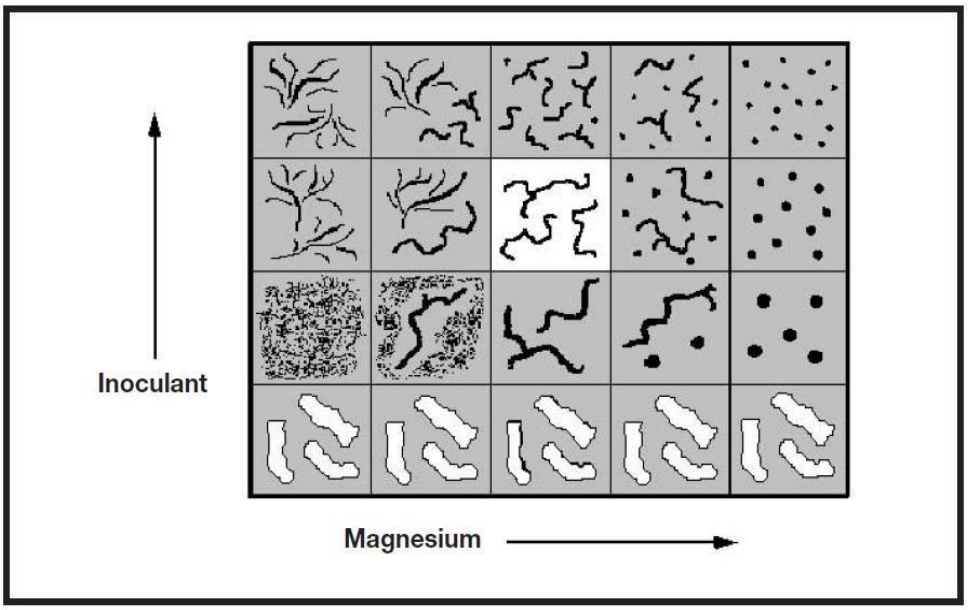

Figure 11: Sensitivity of Compacted Graphite Iron to both magnesium and inoculant [3]

3 SOLIDIFICATION

Cast iron is a group of iron-carbon alloys with a carbon (C) content greater than 2%, and are characterized by eutectic solidification. Hypoeutetic Cast Irons present a C content below the eutectic concentration, for which their solidification begins with the crystallization of the iron rich phase austenite (ɣ). On the other hand, hypereutetic Cast Irons have a C content that exceeds the eutectic concentration, and their solidification starts with the crystallization of the carbon rich phase. The basic Cast Iron characteristics can be described through the use of the phase diagram (figure 12) [11].

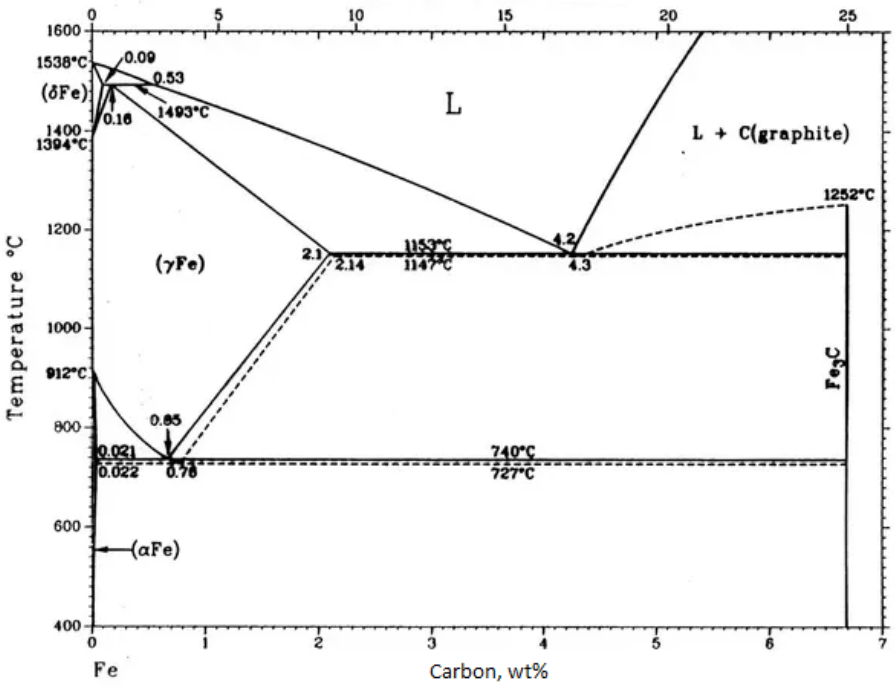

Figure 12 - Stable and Metastable Fe-C equilibrium phase diagram [11].

During its solidification, the liquid transforms into ɣ and a carbon rich phase. This is named as the eutectic reaction, and occurs under the eutectic temperature. Graphite (G) is the thermodynamically stable carbon rich phase, whereas cementite (Fe_3C) is the metastable one. Fe3C can be formed instead of G if the migration of C is not fast enough [11].

According to their fracture surface, Cast Irons can be classified as either White Cast Irons – when the metastable reaction is predominant; or as Grey Cast Irons – when the graphitic irons have a darker fracture surface.
Due to the fact that Fe3C is of hard and brittle nature, for most applications the stable eutectic transformation is desirable. Also, the fact that G induces and expansion upon its precipitation from the melt can compensate the shrinkage associated with the austenite transformation. Graphitic Cast Irons contain at least one graphitizing agent, usually Silicon (Si), in order to promote the stable eutectic reaction under practical cooling conditions [12].

For decades, the foundry industry has been treating Cast Iron melts with several additives for numerous practical benefits, with various commercial inoculants being currently available. Many of these are based on FeSi but also contain additions of elements like Al, Ba, Ca, Mn, Sr, Ti or Zr, that promote the heterogeneous nucleation. The alloying elements used for this purpose will suppress the metastable eutectic reaction, by lowering the equilibrium temperature of the metastable in comparison to the stable eutectic. On the same note, the alloying elements that have the opposite effect of promoting the metastable eutectic reaction are named as carbide stabilizers [11, 13].

3.1 Solid State Transformation

When the solidification is completed and before the room temperature is reached, a solid-state transformation generally occurs, where the ɣ is converted into ferrite (α)+G, with the G normally growing on existing particles. At this stage, the Fe3C metastable phase may also be formed, through the reaction ɣ→α+Fe3C+G, which usually results in a fine matrix microstructure called pearlite [11].

Aside from graphitizing agents and carbide stabilizers, some alloying elements can be classified as ferrite or pearlite stabilizers, if they promote the formation of these two phase as a product of the solid state transformation [11].

4 CGI APPLICATIONS

Compact Graphite Iron is an intermediate material between grey iron and ductile iron. The most obvious use of CGI is in applications where the strength of grey iron is insufficient, but in which a change to ductile iron is undesirable, since this last one has less favorable casting properties than CGI.
Early applications of CGI include high speed train brake disks, where grey iron experienced surface cracking failure, while the high elastic modulus and low thermal conductivity of ductile iron led to excessive deformation [7].

As shown in Figure 13, CGI provides a good intermediate balance between cracking and distortion, making CGI ideal for applications with simultaneous thermal and mechanical loading [7].

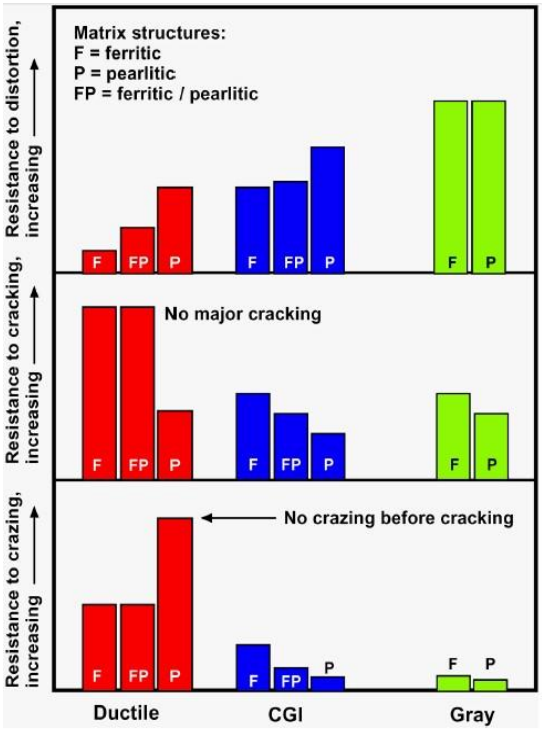

Fig. 13: Comparison of different properties between CGI, grey iron and ductile iron [7]

Some examples of applications of CGI in the automotive industry include bed plates for large diesel engines, crankcases and gearbox housings [10].

The largest industrial application by weight of CGI is for ingot moulds weighing up to 60 tons. The life time of ingot moulds made of CGI is 20 to 70% higher than that of those made of grey iron [10].

Modern car and truck engines require that manifolds work at a temperature around 500 °C. At these temperature, grey iron manifolds are prone to cracking, while ductile iron manifolds tend to warp. CGI manifolds warp and oxidize less which leads to a longer life time [10].

5 DEFECTS IN CAST IRON

The interaction between the liquid metal and the mould during casting solidification is responsible for several shrinkage-induced defects, which are normally termed as shrinkage cavities and shrinkage porosities [14].

The quality of the casting depends on whether or not the liquid metal flows into the solidified regions, in order to compensate the mass deficit that results from solidification contraction. In case this mass deficit is not properly fed, shrinkage defects are produced [14].
The classification and definitions presented in Figure 14 are the ones used throughout this research work.

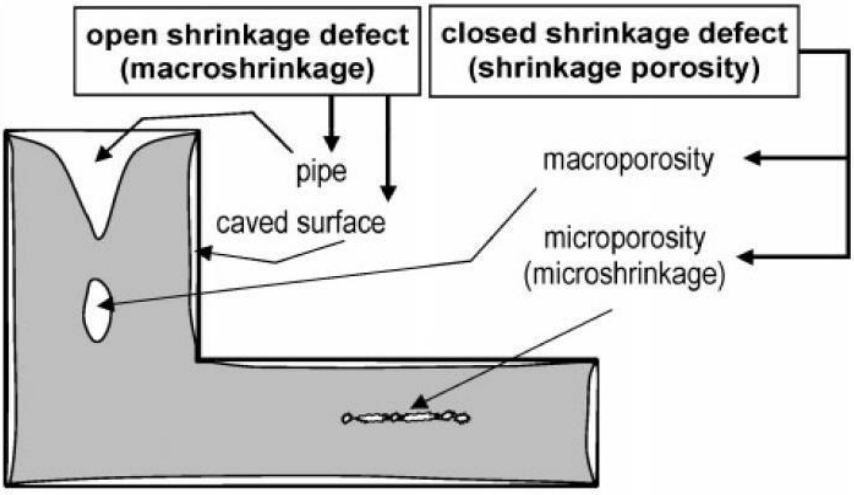

Figure 14 - Definition and classification of Shrinkage Defects [14].

Shrinkage defects that are open to the atmosphere (also called shrinkage cavities) are the consequence of metal contraction during solidification. In this case, the mass deficit that is produced by shrinkage, is then compensated by the atmospheric gases. This process is independent of the gas content of the metal and does not require gas pore nucleation and growth [14].

On the contrary, closed shrinkage defects correlate well with nucleation and growth of pores, and thus seem to depend on the impurity level and the amount of gas dissolved in the metal [14].

5.1 Shrinkage Defects

Pipe formation is the direct result of the mass deficit produced by metal contraction. In order to avoid macro shrinkage formation, the progressively solidified area, the solidification front, needs to be continuously fed with liquid metal [14].

As the metal solidifies, the feeding ability of the liquid tends to continuously decrease. The solid grains are formed in the liquid after the solidification starts, and with this, the viscosity of the melt is increased, causing the flow velocity to gradually decrease. As solidification proceeds, dendrite coherency eventually occurs, and a fixed solid network is formed, leading to a further decrease in feeding capacity [14].

Contractions of cast irons can generally be categorized in three types, occurring at different times during solidification. These are **liquid shrinkage**, **liquid to solid** and **solid shrinkage** [9].

- **Liquid shrinkage** is the first shrinkage step which is the consequence of heat loss in liquid metal.
  High pouring temperatures tend to enhance shrinkage defect formation. In general, if the liquid metal is well supplied, shrinkage defect would not arise at this stage [9].

- **Liquid to solid stage** is the primary source for shrinkage porosity formation. While the temperature decreases, the solid phase is formed, with the viscosity being increased.
  As this happens, it gets more difficult for the melt to reach the isolated voids, since the dendrites start to form and these voids get entrapped between the dendrite arms [9].

- **Solid shrinkage** occurs after solidification, when the final shape of casting is achieved.
  This phenomenon should be taken into consideration while designing the pattern [9].

5.2 Porosity Defects

While the liquid phase is cooling down and solidifying, a significant amount of the dissolved gas is rejected by it. If a critical pressure is overcome, a gas bubble is formed, leading to the initiation of porosity. If the gas bubble is formed in the liquid, it floats. In case this gas bubble does not reach an open liquid surface it interacts with the solid/liquid interface eventually forming gas porosity. This is not a shrinkage defect [14].

If the gas bubble is formed in the later stages of solidification, after dendrite coherency, it becomes entrapped in the dendritic network and small local cavities are nucleated, which are termed microporosity or gas entrapments [14].

5.2.1 Gas Porosity

The interaction of a gaseous inclusion with the S/L interface is rather complex. When the pore is relatively far from the S/L interface the mechanism that favors pore growth is hydrogen diffusion through the liquid phase. The growth rate increases as the S/L interface approaches the pore. The pore takes an ellipsoidal shape as the interface gradually involves it [15].

If the interface is non-planar the pore is entrapped by the solid. In either case the pore has a spherical or elliptical shape (Fig. 15). Its size may be of the order of micrometers – millimeters [14].

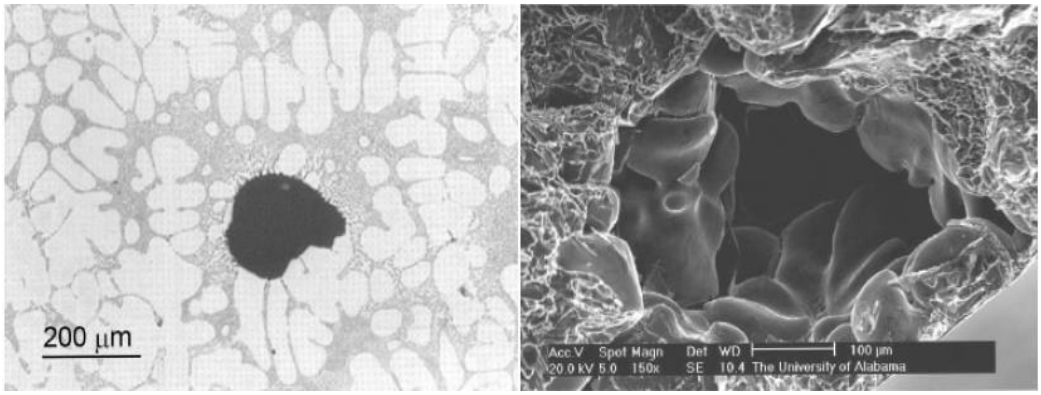

Figure 15 - Optical micrograph and SEM image of a typical gas pore [14].

5.2.2 Microporosity

The defects that have a dendritic shape, rather than a spherical one, are termed microporosity or microshrinkage. This type of porosity takes the shape of the interdendritic liquid that remains just before eutectic solidification (Fig. 16) [16].

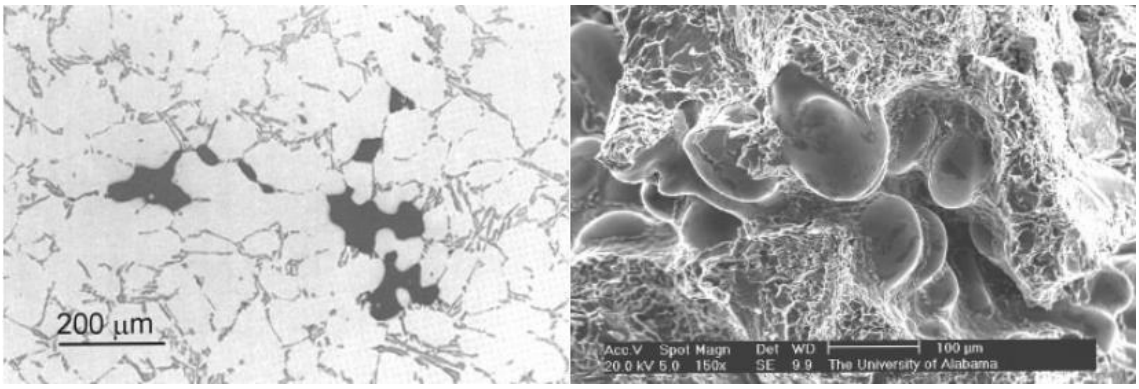

Figure 16 - Optical micrograph and SEM image of interdendritic microshrinkage [16].

The current understanding of how microporosity is formed is that the melt flows towards the region where shrinkage is occurring, until the flow is blocked, by either the encounter of solid metal or by a solid or gaseous inclusion. When a microporosity appears in the later stages of solidification, after dendrite coherency, it is entrapped in the dendritic network [16].

6 HYDROGEN AND NITROGEN

Nitrogen and hydrogen gases are quite problematic when it comes to their influence in cast irons, with hydrogen being more active in porosity formation [9].

Hydrogen mainly derives from residual water and organic materials. The sources of water could be from the raw material, from the humidity in the air or even from humidity in the mould. This last one is considered to be the main source of hydrogen, since the mould highly reacts with the molten metal. This reaction leads to the dissociation of water into H_2 and O_2 and in a further dissolution of hydrogen into the liquid metal [1].

The hydrogen solubility limit is very dependent on the temperature, with it increasing as the temperature increases. In the solid state, the solubility depends on the phase state of the iron - it is higher in austenite than it is in ferrite [1].

Atmospheric Air contains 79% nitrogen, and since the molten iron is in constant contact with the air, this is one of the main sources that leads to the presence of Nitrogen in the melt. Other possible sources of nitrogen are the resin binders and the scrap iron [1].

Nitrogen is always present in cast irons to some extent, promoting pearlitic structure and increasing tensile strength. Optimal N_2 level is between 40 to 90 ppm and higher levels might result in defect formation [9].

In contrast with Hydrogen, the solubility of Nitrogen only slightly increases when temperature is increased [1].

7 NONDESTRUCTIVE METHODS

Throughout the last decade the use of non-destructive testing techniques for the evaluation of material structures and the prediction of material behaviour has grown extensively. These techniques include X-ray, eddy current, neutron scattering, electromagnetic, and ultrasonic characterization of materials, among others [17].

The ultrasonic technique has been applied rather extensively. In addition to the determination of material parameters such as elastic modulus and density, it is also commonly applied for the measurement of the grain size, the degree of porosity and the amount of second-phase particles of several casting materials [17, 18].

7.1 ULTRASOUND ON THE DETECTION OF CASTING DEFECTS

When it comes to the detection of porosity defects by a non-destructive technique, the main problem is that their size is usually near the limits of detections for most of the non-destructive testing methods. There is a need for a reliable and cost effective test which can be applied to different castings. Ultrasound testing is widely used for finding internal defects such as shrinkage porosity in cast iron [19, 20].

The common equipment, used in ultrasonic flaw detection, electronically generates a high frequency beam of vibrations, and sends these vibrations into the tested cast. Any discontinuities such as cracks, inclusions and seams will influence the vibration. Discontinuities can be determined by measurement of the elapsed time between the initial and the received pulse. Thickness, grain size and density variations can also be determined [19, 20].

One of the primary ultrasonic techniques most commonly applied for the detection of internal defects in cast irons is the “Pulse Echo” technique. This was the method used in this study [20]:

7.1.1 Pulse Echo

Basically, in pulse echo the total transmitted time is measured. In a standard sample, for a given set of conditions, it takes a total time, $t_T = t_1 + t_2$, for the pulse to be transmitted and received as shown in Figure 18.

In the case of a sample with an inclusion or a crack, the total transmission time, t^*_T, is less than the standard [21].

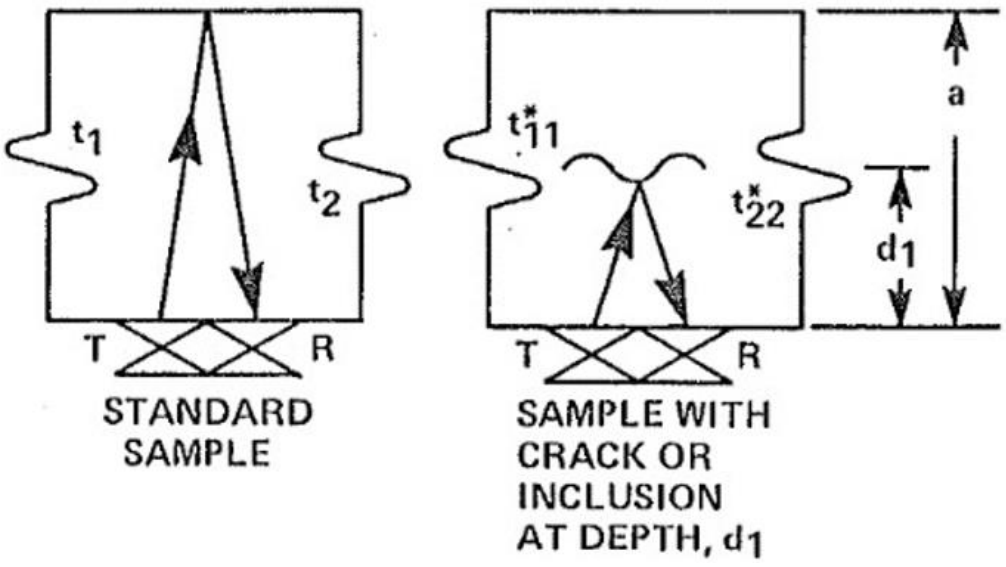

Figure 17 – Pulse Echo Testing [18]

8 COLOR ETCHING

In order to reveal the microstructure of various materials used by the foundry industry, the color etching technique is commonly applied, helping with the identification of different metallographic phases [22].

The method of film deposition by chemical etching is one of the techniques for obtaining tints through color etching. It is based on the use of a specific etching reagent that can adequately tint the different phases, which leads to a better metallographic analysis [23].

Through the light interference effect, the thin film left on the surface by the color etchants is revealed in different tints, according to the local film thickness. The formed film must be within a certain thickness range, so that the coloration is properly displayed. Figure 18 shows the interference effect involving the film and the metal surface [23].

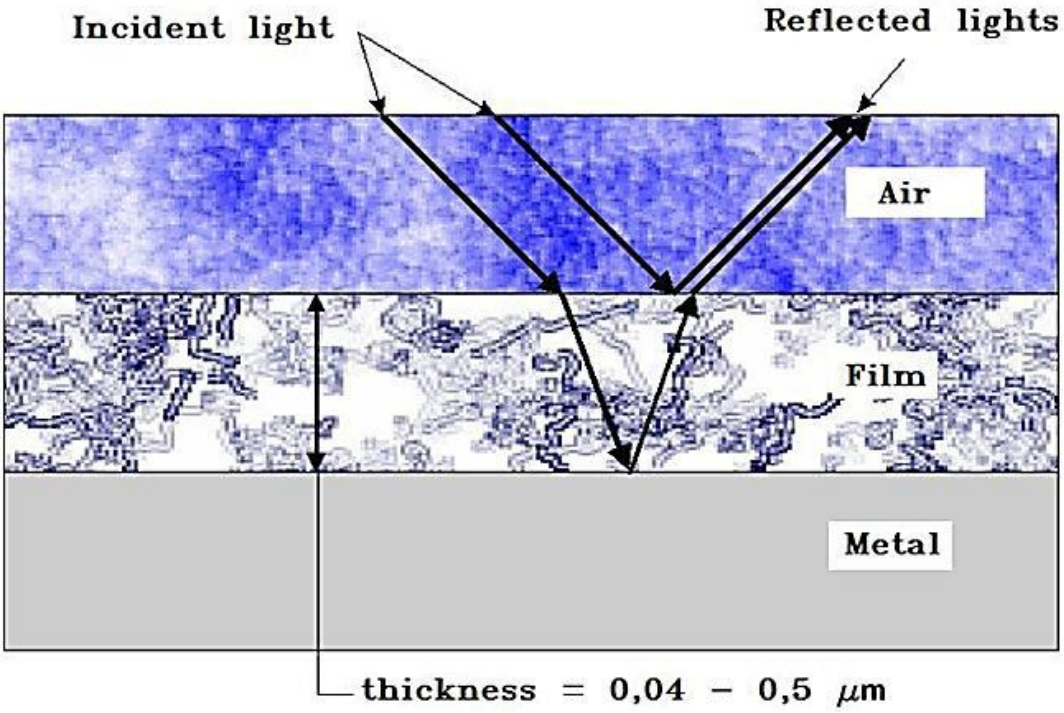

Figure 18 – Representation of the Principles behind Color Etching [24]

For the case of cast iron's microstructural investigation, it can be very helpful to analyse the silicon segregation pattern revealed. This is possible by the use of reagents sensitive to silicon segregation which are discussed as follows [22].

Since the silicon segregates into the austenite phase during solidification and it is gradually segregated from the liquid, the color pattern caused by thin-film interference can assimilate the solidification chronology of the matrix [23].

Due to the fact that silicon displays a behaviour of inverse segregation, it tends to segregate into the austenite. This phase is not detected in the microstructure by usual chemical dissolution techniques [25].

A good way to reveal the austenite pattern in the microstructure is by the use of etching reagents sensitive to silicon that form silicon oxide films. These thin films act as interference layers that react to the different alloying elements present in the sample, without attacking its polished surface. This phenomenon makes it possible to characterize the segregation in the structure [25].

The main challenge with the use of etching techniques is to define the accurate time for getting the best information out of the analyzed microstructure [23].

This etching time will depend on the microstructural composition, the size of the etched samples, and the working temperature. The etchant is normally heated up close to its boiling temperature, which can lead to a change in composition through evaporation of the solution. The whole etching process should therefore be performed as fast as possible [23].

CHAPTER 2

This chapter includes the description of the various experiments that were performed, with the intention of obtaining results that could be useful for this study.

9 EXPERIMENTAL PROCEDURE

For this work, 27 samples of Compacted Graphite Iron were obtained from a central region of casted components. If porosity was present in them, it was expected to be formed in that region. As it is seen in figure 19, the components had a certain geometry where the melt flows down from a vertical feeder, with 5 other separate arms perpendicular to one another.

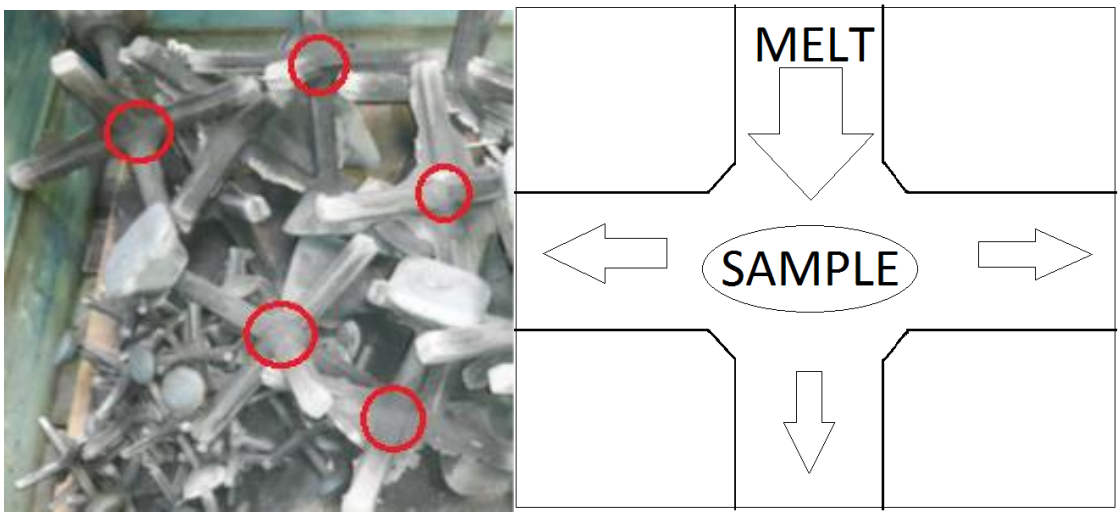

Figure 19 - Some examples of the central position of the CGI samples, where the arms coincide in each component, and a basic replication of the directions of the feeding process on the left.

The geometry of the different casted components is presented in Figure 20 in a 3D view.

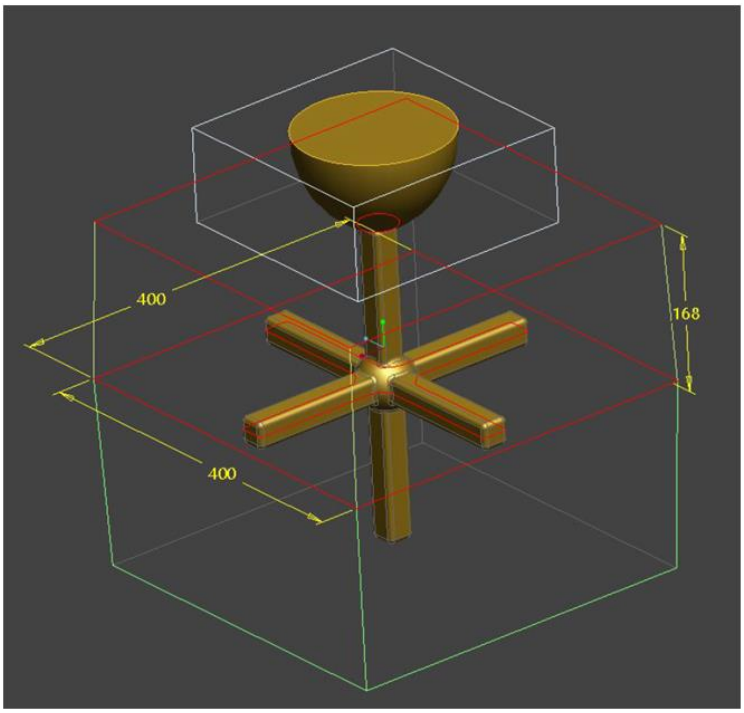

Figure 20 – Geometry of the casted samples. Φ=60 mm, where Φ represents the diameter of the central part.

The components were casted in furan sand moulds (Figure 21) with different chemical compositions and different amounts of inoculant and Magnesium (Mg). Table 1 shows the chemical composition of the hypoeutetic CGI studied in this work.

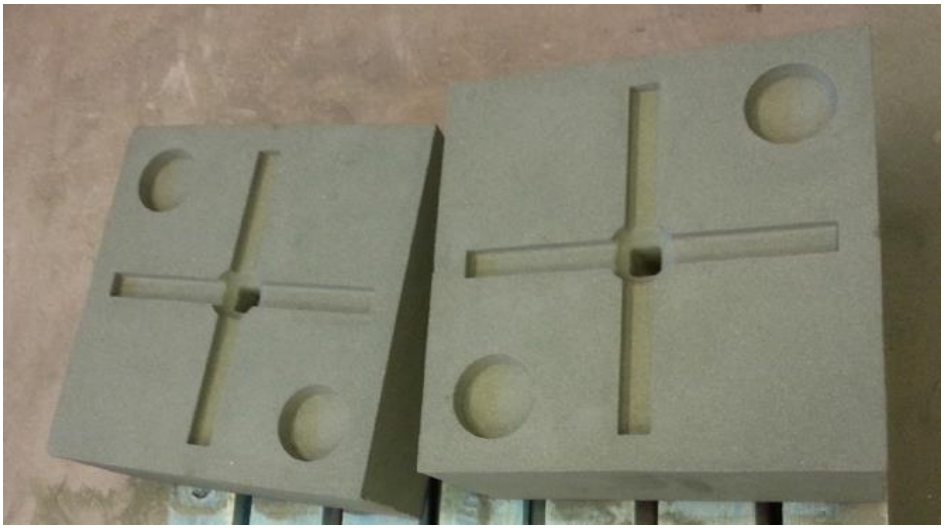

Figure 21 – Sand mould for the sample with Φ=60 mm

Table 1 - Chemical composition of the investigated CGI

Alloy ID	C	Si	Mn	P	S	Cu	Ti	V	Sn	Mg	Cekv
1-1	3,625	1,890	0,352	0,032	0,013	0,92	0,005	0,001	0,062	0,006	4,113
1-2	3,599	1,930	0,350	0,032	0,013	0,92	0,005	0,001	0,064	0,008	4,098
1-3	3,673	1,958	0,351	0,033	0,013	0,93	0,005	0,001	0,064	0,005	4,179
1-4	3,689	1,951	0,346	0,032	0,013	0,93	0,005	<0,001	0,064	0,006	4,193
1-5	3,672	1,920	0,344	0,031	0,014	0,94	0,005	0,001	0,063	0,006	4,168
2-1	3,676	1,848	0,319	0,032	0,014	0,92	0,005	<0,001	0,061	0,008	4,154
2-2	3,650	1,922	0,323	0,033	0,013	0,92	0,005	<0,001	0,063	0,013	4,147
2-3	3,683	1,893	0,322	0,034	0,014	0,92	0,006	<0,001	0,063	0,013	4,173
2-4	3,678	1,943	0,320	0,032	0,013	0,92	0,006	<0,001	0,062	0,015	4,180

Cekv=[C]+¼[Si]+½[P]

The analyzed region was similar for all the studied samples, which was on the central part, where most of the porosity was formed. Figure 22 illustrates some of the studied samples, with their respective added Mg and Inoculant contents according to each lot of samples. The porosity defects that appeared in each sample are highlighted and will be discussed in a later stage of this report.

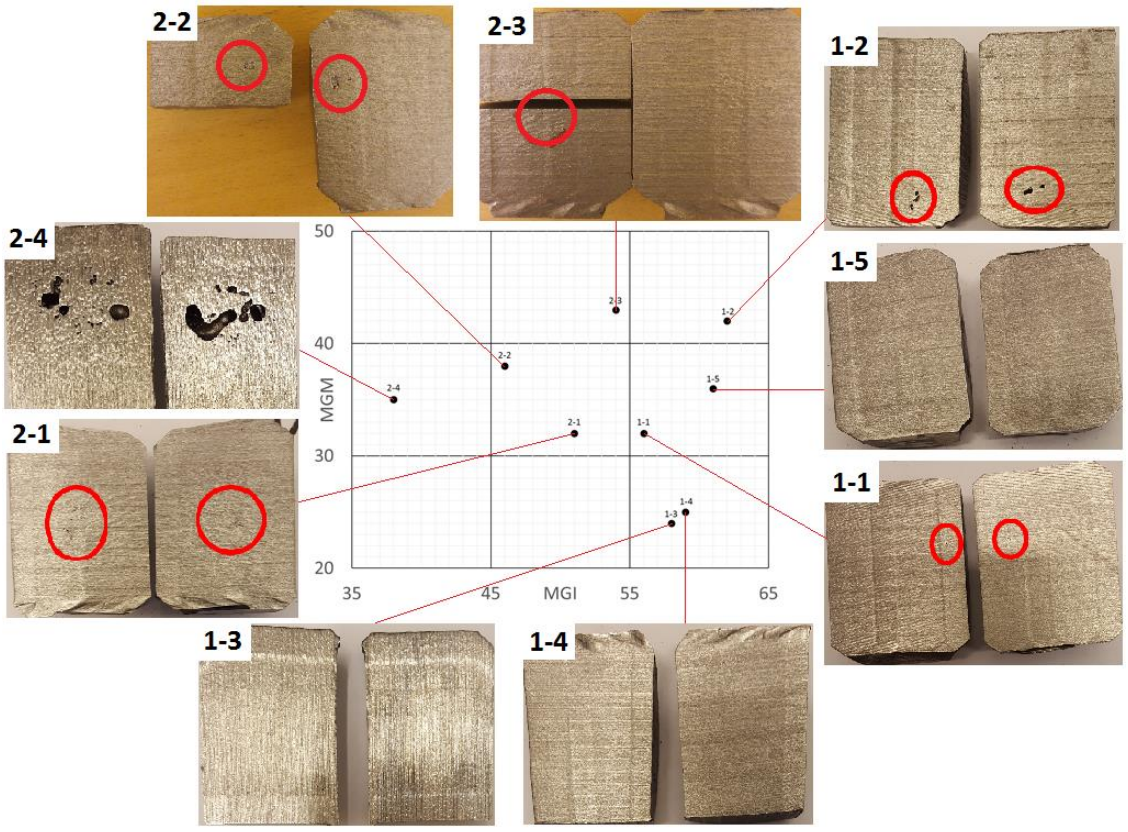

Figure 22 - Magnesium and Inoculant compositions defined by Sintercast for each samples from the respective CGI components.

9.1 ULTRASOUND ANALYSIS

The reason why the ultrasound technique was used as a first step, was because it is a good method to predict the location of internal defects, without damaging the samples. This allowed us then to cut the samples through the transversal section that would reveal the internal surface of the porosity.
While measuring the samples through ultrasound, some variations usually occured. These variations were caused by both the fact that the samples differ from each other, as well as due to the measurement method having its flaws.
This leads to the assumption that measurements of the same samples might not result in identical responses. What that means is that it is crucial to identify and minimize the sources of variations when performing a statistical study, in order to achieve consistent results.

For this study, the ultrasonic system consisted of a Panametrics EPOCH4B Digital Ultrasonic Flaw Detector pulser/receiver and an ultrasonic transducer. Figure 23 schematically illustrates the system used.

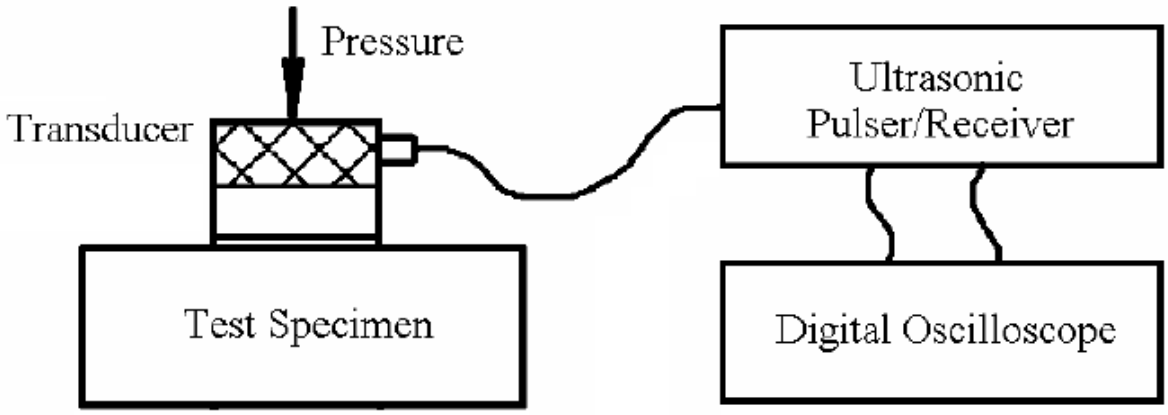

Figure 23 – Schematic illustration of the Ultrasonic Equipment used in this study

The transducer was powered by the pulser/receiver, and it was aligned vertically on the samples. The ultrasound signal was both sent and then received by the same transducer. The transducer had a diameter of 17.7 mm and the frequency used was of 4 MHz.

In order to assure th at the samples were being accurately measured, multiple measurements were performed. Also, the coupling pressure applied on the transducer on top of each sample was maintained constant, so that the ultrasound signal was kept consistent.
These samples were then cut according to the Ultrasound Analysis, through vertical and horizontal sections where the porosity was predicted. The analyzed areas showed either big uniform gas pores, small pores with irregular shape or no porosity at all.

9.2 GRAPHITE CHARACTERIZATION

Each sample was adequately prepared through several steps of grinding and polishing. In order to study the influence of graphite nodularity level on porosity formation, graphite characterization was a crucial step in this work.

The first stage in the investigation of graphite morphology consisted on collecting several images from the surface of the polished samples, through the use of an optical light microscope. Each picture was captured using the 5x microscope objective lens. A total of 25 images were taken per studied surface, whose total area had a minimum of 4 mm^2.
The analyzed samples had to be properly polished in order for the shape and size of the graphite to be clear in the observed images.
These images would cover the whole surface of the samples, being adequately spread out from each other, and from areas both near and far away from the porosity, if there was any.

The image analysis was followed by the graphite characterization of each CGI samples, through the measurement of their percent nodularity, which characterizes the graphite microstructure.

The norm ISO 16112 states that in order for the samples to be classified as being CGI, they must show a minimum of 80% of the graphite particles in the

vermicular shape (shape III according to ISO 16112), while the remaining 20% of the graphite particles should be of shapes VI or V.

Flake (lamellar) graphite (shapes I and II) is not meant to be formed in the CGI structure. Figure 24 illustrates the different types of graphite form mentioned.

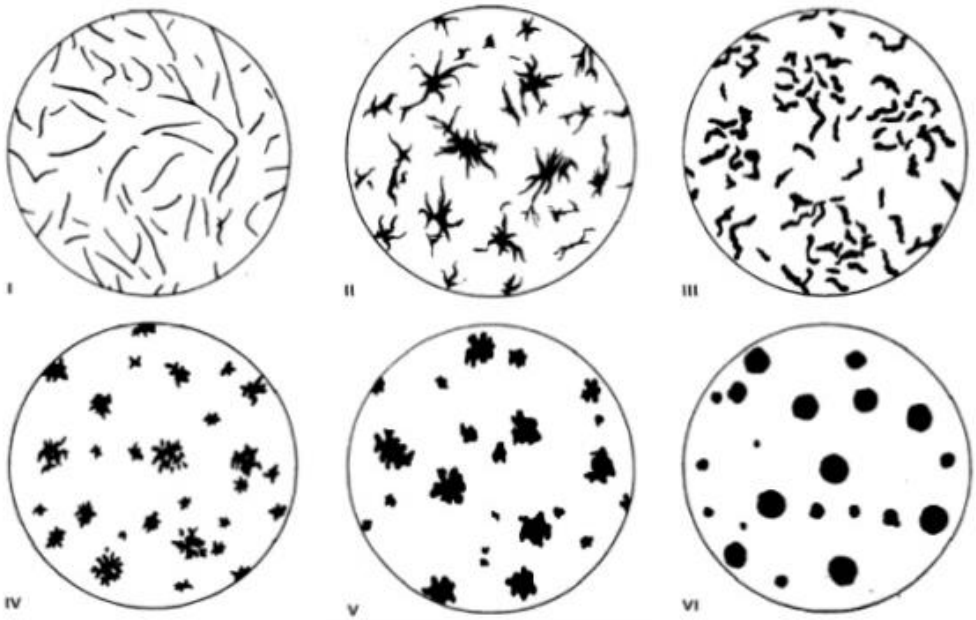

Figure 24 - Standard Graphite Shapes in Cast Irons according [29]

The calculation of nodularity through image analysis is based on the roundness-shape factor, which is defined according to the following equation (figure 25).

$$\text{Roundness} = \frac{A}{A_m} = \frac{4 \times A}{\pi \times l_m^{\,2}}$$

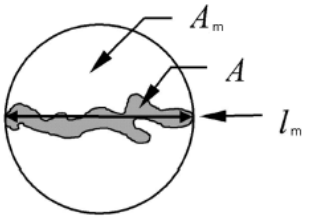

Key

A_m area of circle of diameter l_m

A area of the graphite particle in question

l_m maximum axis length of the graphite particle in question = maximum distance between two points on the graphite particle perimeter

Figure 25- Equation and Illustration of How the Roundness-shape Factor is Measured [29]

This analysis considers graphite particles larger than 10 µm, which are either spheroidal graphite (shape VI), intermediate form (shapes V and IV) or vermicular graphite (shape III), as it is described in table 2.

Neither flake graphite nor particles with a maximum axis length of less than 10 µm are not included in the measurement.

Table 2 - Graphite Particle Classification in Terms of Roundness-shape Factor [29]

Roundness-shape factor	Graphite form
0,625 to 1	Nodular (ISO form VI)
0,525 to 0,625	Intermediate (ISO forms IV and V)
< 0,525	Compacted (ISO form III)
Flake graphite particles and graphite particles with maximum axis length less than 10 µm are not included in the analysis.	

The percent nodularity is then calculated according to the following equation [29]:

$$\text{Percent nodularity} = \frac{\sum A_{\text{nodules}} + 0{,}5 \times \sum A_{\text{intermediates}}}{\sum A_{\text{all particles}}} \times 100$$

Where A_{nodules} and $A_{\text{intermediates}}$ represent both the areas of particles classified as Nodular Graphite and as Intermediate forms of graphite, respectively.

$A_{\text{all particles}}$ represents the area of the graphite particles larger than 10 µm.

The graphite morphology and the percent nodularity are obtained using the image analyzing software *Olympus Stream*, which is linked to the optical light microscope.
The software analyzes and classifies the graphite according to its morphology.

9.3 COLOR-ETCHING

Most microstructural details are not visible in the samples that are only polished. In order to obtain information about their solidification structure, the samples were then color-etched.

The study of the Si segregation in Compacted Graphite Iron, possible through the use of this method, was conducted in order to understand the solidification of this type of cast iron.

The etching technique was performed with a reagent of 10g of NaOH, 40g of KOH, 10g of Picric Acid and 10 ml of distilled water, at a temperature of around 100ºC.

For this experiment, the etching time for each sample was between 10 and 15 minutes. The samples were then cleaned and dried, followed by their examination through optical microcopy. If necessary, the samples were reintroduced in the reagent for a few minutes until the desired coloring was achieved.

The etched surfaces were then captured digitally using an optical microscope at 2,5x objective lens magnification. The images were stitched into panoramic micrographs using the software Image Composite Editor, and it is displayed in figure 26.

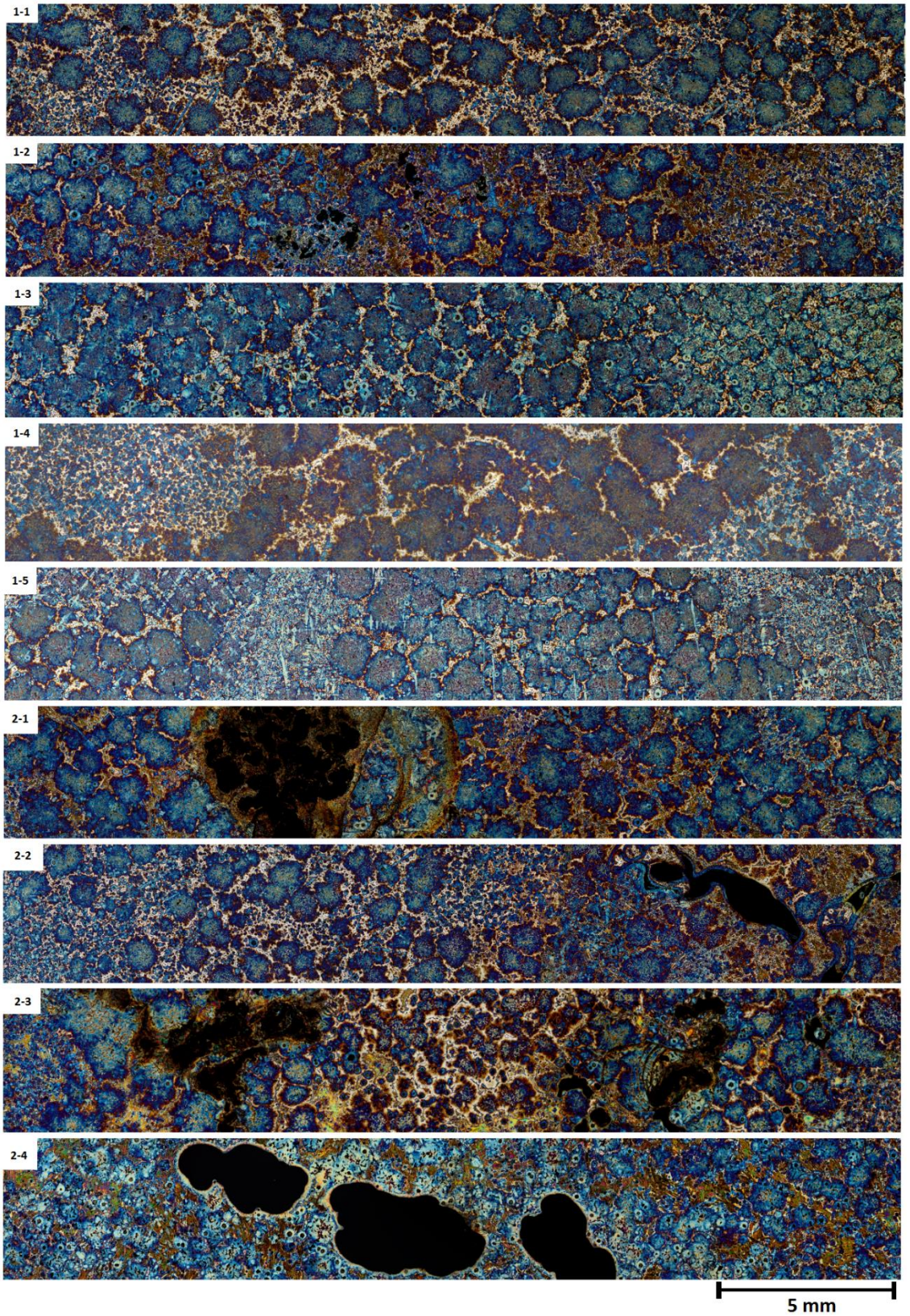

Figure 26 - Panoramic images of some of the etched CGI samples out of each different lot, taken from the central area of the samples and where the porosity was located.

CHAPTER 3

This chapter addresses the several results obtained in this work, with a thorough discussion of the same.

10 RESULTS AND DISCUSSION

10.1 ULTRASOUND ANALYZES

The ultrasound evaluation originated the results that are presented in table 3. These results state whether or not each sample had any kind of porosity, which would interfere with the signal sent and received by the transducer.

Table 3 - Comparison between the ultrasound evaluation performed in each sample and their level porosity

LOTE	SAMPLE NUMBER	Ultrasonic Evaluation (0:No, ½:Maybe, 1:Yes)	POROSITY
1-1	1	0	No
	10	0,5	Shrinkage Porosity
	13	1	Gas Porosity
1-2	7	0,5	Shrinkage Porosity
	9	0	No
	11	0	Shrinkage Porosity
1-3	3	0,5	No
	4	0,5	No
	8	0	No
1-4	2	0	No
	5	0	No
	6	0	No
1-5	12	0	No
	15	1	No
	16	0	Shrinkage Porosity
2-1	17	0	Shrinkage Porosity
	19	0	Shrinkage Porosity
	20	1	Shrinkage Porosity
2-2	21	1	Shrinkage Porosity
	22	1	Gas Porosity
	23	0,5	Gas Porosity
2-3	14	0,5	Shrinkage Porosity
	24	0,5	Shrinkage Porosity
	25	0	Shrinkage Porosity
2-4	18	1	Gas Porosity
	26	1	Gas Porosity
	27	1	Gas Porosity

By moving the transducer across the surface of the sample, the ultrasound signal was supposed to be fairly constant.
Whenever any kind of interference occurred, that area would be marked and a transversal cut would then be made across that section to see if in fact there was some kind of porosity.

The samples were evaluated as either:

(1) - Positively having porosity, if the discrepancy in the ultrasound signal was very clear in a certain area;
(0,5) - Possibly having some porosity, if the signal showed some unclear interference;
(0) - Or not having any porosity at all, if the signal was constant throughout the all surface.

Despite the fact that the analyzed ultrasound signal was not always as clear as desired, in most cases it gave an accurate evaluation of the porosity level in all 27 samples.

- In 5 Samples it was NOT expected any porosity, but it ended up appearing.
- In 3 Samples it was expected porosity, but there was none.
- In 7 Samples it was NOT expected any porosity, and there was none.
- In 12 Samples it was expected porosity, and it showed up.

This results show that the ultrasound analyzes on the prediction of internal porosity had a reliability rate of just over 70%.

This degree of accuracy goes to show that the evaluation is not as precise and clear as desirable, although it could be more accurate if more advanced equipment was to be used. Since the tests were performed with a simple ultrasound device, most of the testing judgement was up for the user to make, which obviously leads to some error in the results.

10.2 COLOR ETCHING

10.2.1 Microstructure

The difference in the etching colors represents the different local silicon concentrations. The highest Si content is revealed in blue, whereas the lowest Si content shows up in light brown.

For the studied color etched CGI samples, the areas tinted in blue, and therefore with the highest Si segregation, are the primary austenite (dendrites), the secondary austenite (eutectic colonies) and the areas around the graphite spheroids.

On the other hand, the areas tinted in light brown are representative of the last solidified regions.
The darker brown color at the border of the eutectic colonies shows that the Si concentration is slightly higher close to the cells.
Figure 27 illustrates the surface of one of the color-etched samples, captured with optical microscopy.

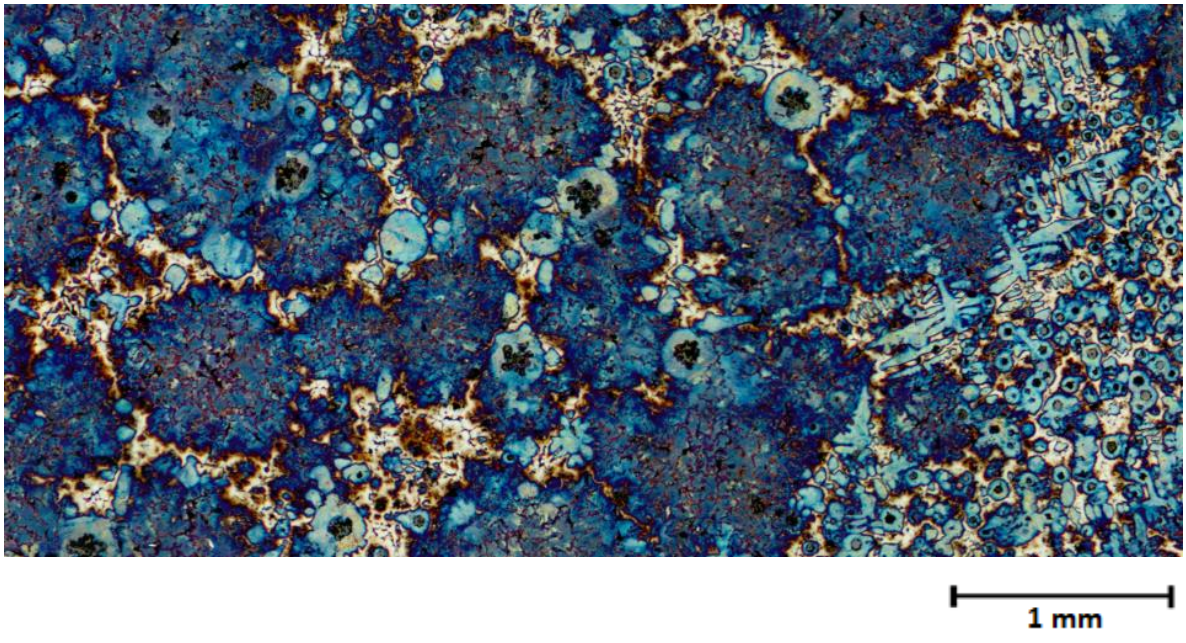

Figure 27 – Microstructure of a color etched CGI sample

The eutectic cells are easily distinguishable, having a spheroidal shape, with austenite and vermicular graphite growing within them. Several graphite nodules are shown in between the dendritic arms.
During the solidification of cast irons, the Si tends to be concentrated in the austenite phase while it segregates from the melt. As solidification proceeds, the Si content in the liquid gradually decreases, leading to the interdendritic areas and the last solidified areas to contain the lowest amount of Si.

The primary austenite and the graphite nodules nucleate and grow independently from each other along the liquid. Eventually, the graphite precipitates become covered with the austenite phase, as they come in contact with the gradually formed solid phase.

10.2.2 Graphite Nodules

In figure 28, two different types of graphite nodules are identified. It can be seen that the area/shell around the graphite nodules is colored differently in both cases. This shows that the segregation of Si varies between the two types of graphite nodules.

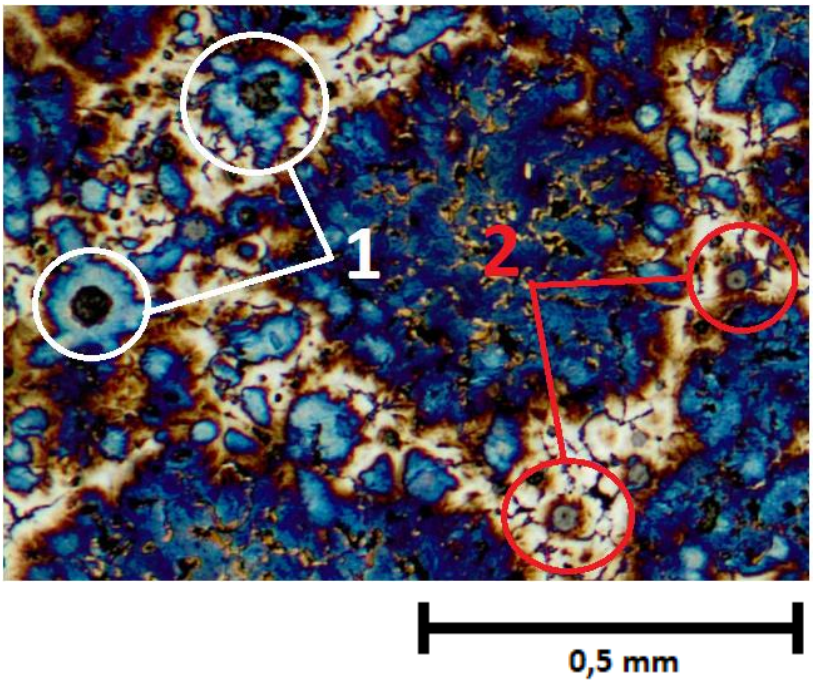

Figure 28 - The two types of graphite nodules are highlighted in this color etched CGI microstructure.

Some of the graphite nodules have a higher Si segregation, which is observed by the blue pattern around them. Whereas, the other smaller graphite nodules are covered by mainly light brown areas, indicative of lower Si contents, which are characteristics of the last solidified regions.

Since these two types of graphite nodules have different sizes, are located in separate regions, and are associated with different Si segregation patterns, it can be assumed that their nucleation and growth occur during different phases of the solidification process.

The spheroidal graphite connected to the areas with higher Si content was supposedly formed at earlier stages of solidification, which allowed enough time for it to interact with the primary austenite.

On the other hand, the spheroidal graphite associated with the lower Si concentration is assumed to have been precipitated at later stages of the solidification. This nodular graphite can appear in the interdendritic areas, which is due to the rejection of carbon from the dendrites during their growth.

Another reason why this type of spheroidal graphite is associated with low amounts of Si segregation is because the Si is progressively being expelled from the melt and segregated towards the austenite, as solidification takes place.

Since these nodules form at later stages of solidification, the Si concentration in the melt is very low by then.

Another key aspect about the microstructure that is visible in figure 29 is the appearance of individual vermicular graphite particles in the last solidified areas, which were nucleated with no contact with the eutectic cells.

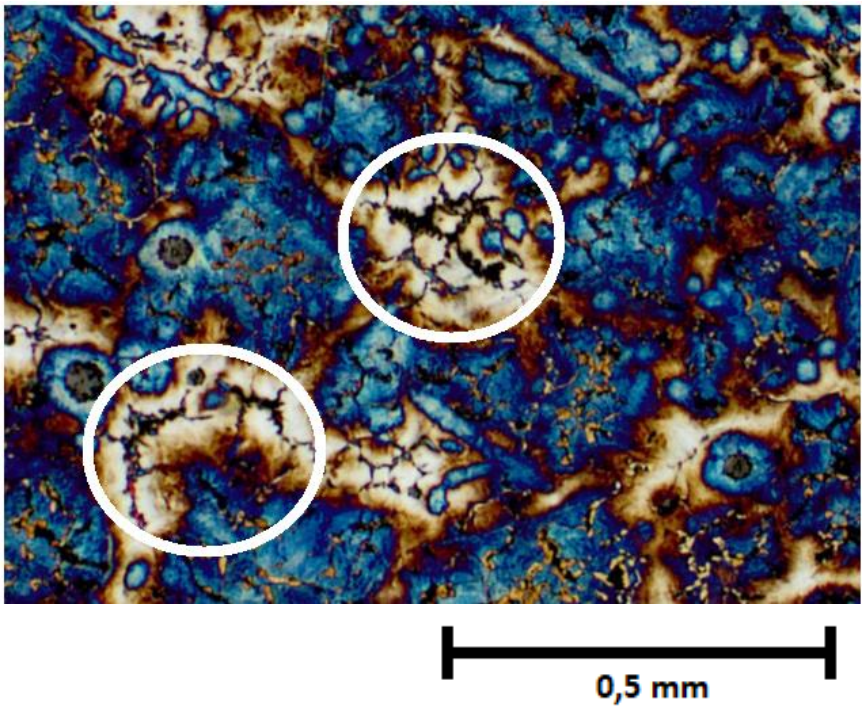

Figure 29 – Individual Vermicular Graphite particles are marked in the last to freeze areas of this CGI microstructure.

10.2.3 White Eutectic - Cementite

The formation of what is defined as white eutectic (cementite) can occur when the solidification rate is too high, and the temperature drops below the metastable eutectic temperature. Therefore, in order to acquire a good thermodynamically stable compacted graphite morphology, specific solidification conditions must be followed [28].

According to the cooling conditions, two different carbide formation cases can be reported [28]:

- There's a tendency for carbide formation in case of a slow cooling rate, aligned with a small number of growing eutectic grains, which is equivalent to low inoculation.
  These carbides are generally formed in the last solidified areas, between the graphite/austenite eutectic cells [28].

- On the other hand, the melt also tends to solidify as white eutectic for higher cooling rates, which is common in components with thinner sections.

  The temperature of the melt drops under the metastable eutectic transformation temperature at the early stages of solidification, leading to the most part of the structure being white eutectic [28].

The solidification of the melt into either cementite or graphite can also be determined by the presence of certain alloying elements, which influence both stable and metastable eutectic transformation temperatures. As previously mentioned, these alloying elements can be classified as being graphitisers, like Si, Cu and Al; or carbide promoters, as Cr, V and Mn are [11].

For this study, the chemical composition was very similar between all the analyzed samples, with all alloying elements with potential graphitizing or carbide promoting properties having close to no difference in contents. So the presence of certain alloying elements would not be a solid reason as for why some samples showed the presence of a carbide phase in their microstructure while others would not.

The white eutectic phase was mainly formed in the last to freeze area, which, as stated above, is correlated to slow cooling rates in that region. This has been reported as being one of the main reasons for the formation of this thermodynamically metastable phase – cementite (Fe_3C) [8].

Figure 30 shows images of two samples where the formation of carbides was common in the last solidified areas.

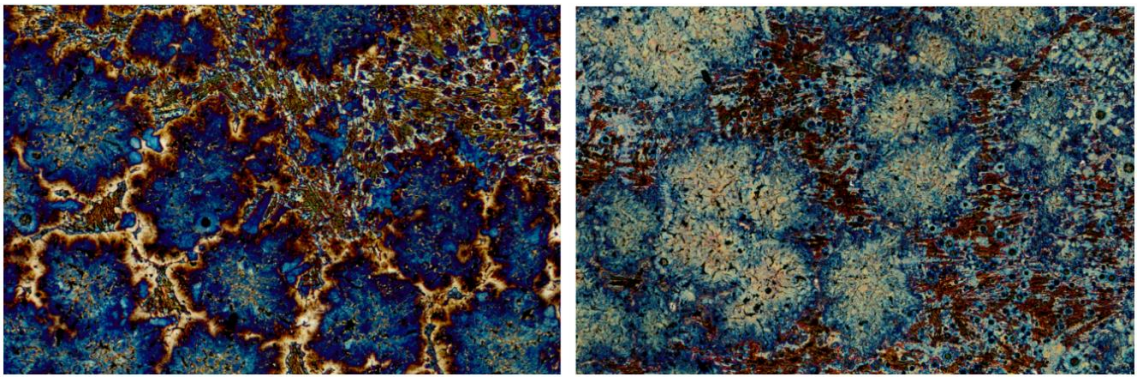

Figure 30 – Two cases in which the white eutectic phase (cementite) is formed in the last to freeze regions.

Since the literature states that low inoculation values have an influence on the formation of these carbides, the main goal was then to see if there was any relationship between the amount of inoculant, the MGI varying parameter, and the appearance of white eutectic.

Although there was a tendency for higher amounts of this metastable phase to be formed in the samples that had higher levels of porosity, there was not a clear relationship with the amount of added inoculant (MGI). The formation of these carbides happened in both samples with high and low amounts of inoculant.

Despite the uncertainty as for why the metastable phase is formed in some of the samples, it is visible that its formation tends occurs in the central area of the samples. This could be justified by the influence that the geometry of the studied components has on their solidification process, that leads to the central area having a low cooling rate. Since this geometry included the "cooling arms" attached to the middle sample (which solidify faster), they could have had a cooling effect on the central region, after they were solidified. This would cause a drastic momentarily high cooling rate in the central region, that would still be at a higher temperature because of the longer solidification time, leading to the formation of this metastable phase [8].

Also, as the areas closer to the edges of the components solidify, and the continuous growth of the eutectic grains occurs there, the overall concentric pressure caused by this factor might drive the metastable eutectic transformation to take place in this central area. This aspect, aligned with the presence of gaseous porosity, could be conductive to the formation of this white eutectic phase.

Nonetheless, this phenomenon can be dependent on several factors, and only further studies could propel better conclusions.

10.2.4 **Porosity**

After analyzing all samples through ultrasound, their level of porosity was then studied. There were two types of pores formed in the samples – either gas pores, bigger in size and with a rounder and smoother surface; or shrinkage pores, with an irregular shape and rough surface.

Figure 31 shows some of the different shapes of porosity found in the studied samples.

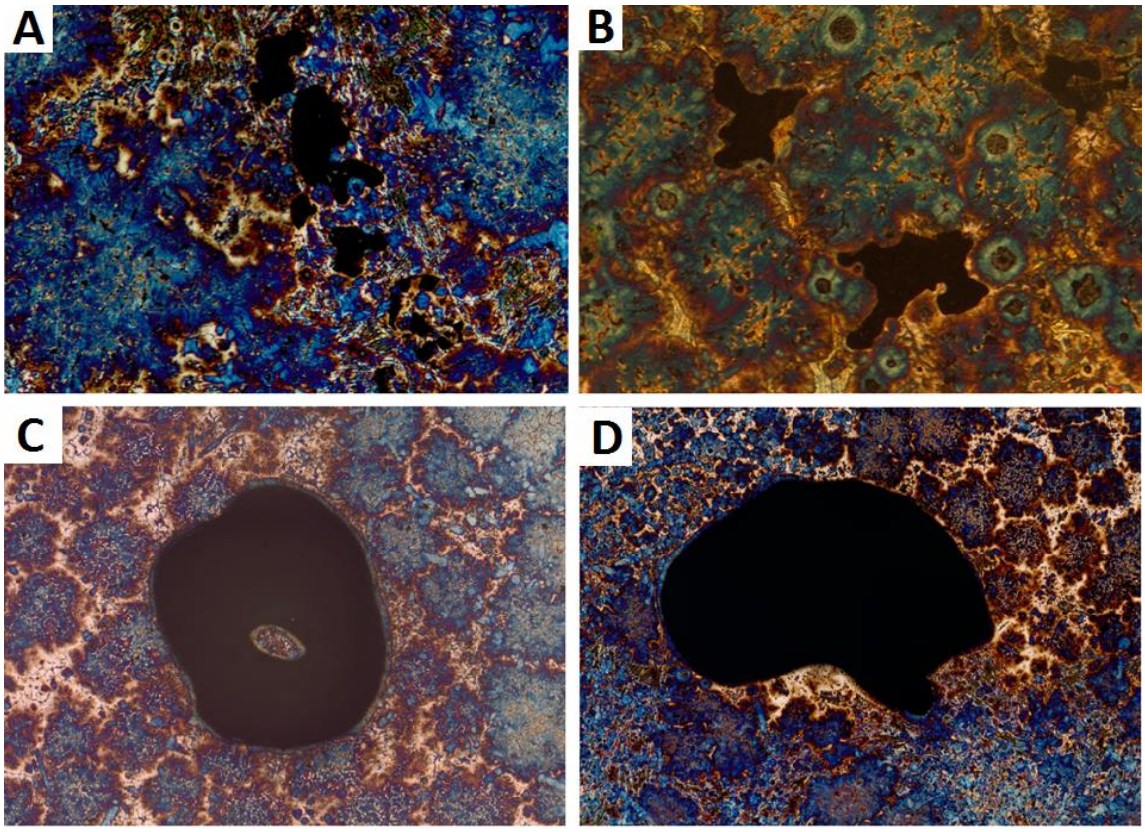

Figure 31 – Shrinkage Porosity (A and B) and Gas Porosity (C and D) present in different CGI samples.

It can be seen that the shrinkage porosity is mainly found in the last to freeze regions, tinted in brown, as both images A and B illustrate. It can be stated that these smaller pores were therefore formed in the later stages of the solidification chronology.

The gas pores on the other hand, presented in images C and D, were found randomly amongst all microstructure, with no clear interface between phases. This leads to the conclusion that these bigger pores were formed in the earlier stages of solidification, and were caused by entrapment of gas within the melt.

10.3 GRAPHITE ANALYSIS - NODULARITY MEASUREMENT

The influence of the amount of nodularity on the porosity in each sample was studied. This was conducted by characterizing the graphite microstructure in all CGI samples according to their percentage of nodularity.
The results from the nodularity investigation are presented in table 4.

Table 4 - Nodularity Percentage, Mg and Inoculant contents and respective amount of Porosity for each sample

LOTE	SAMPLE NUMBER	MGM (Mg)	MGI (Inoc)	PERCENT NODULARITY (%)	POROSITY
1-1	1	33	56	10	No
	10			14	Shrinkage Porosity
	13			8	Gas Porosity
1-2	7	42	62	16	Shrinkage Porosity
	9			22	No
	11			15	Shrinkage Porosity
1-3	3	23	55	8	No
	4			7	No
	8			7	No
1-4	2	26	59	10	No
	5			10	No
	6			14	No
1-5	12	36	61	12	No
	15			14	No
	16			13	Shrinkage Porosity
2-1	17	33	51	18	Shrinkage Porosity
	19			30	Shrinkage Porosity
	20			13	Shrinkage Porosity
2-2	21	44	54	21	Shrinkage Porosity
	22			18	Gas Porosity
	23			30	Gas Porosity
2-3	14	42	55	22	Shrinkage Porosity
	24			23	Shrinkage Porosity
	25			29	Shrinkage Porosity
2-4	18	40	45	23	Gas Porosity
	26			22	Gas Porosity
	27			21	Gas Porosity

With the nodularity levels measured, a comparison with the Magnesium and Inoculant compositions was then conducted. As it is clear in figure 32, the relationship between the amount of nodular graphite in each sample and their added Mg and Inoculant content is far from being linear.

The closest approximation for the influence of these parameters on the percentage of nodularity showed:

- A slight increase in nodularity for higher amounts of Mg addition;
- A small decrease in the nodularity with the increase of added Inoculant.

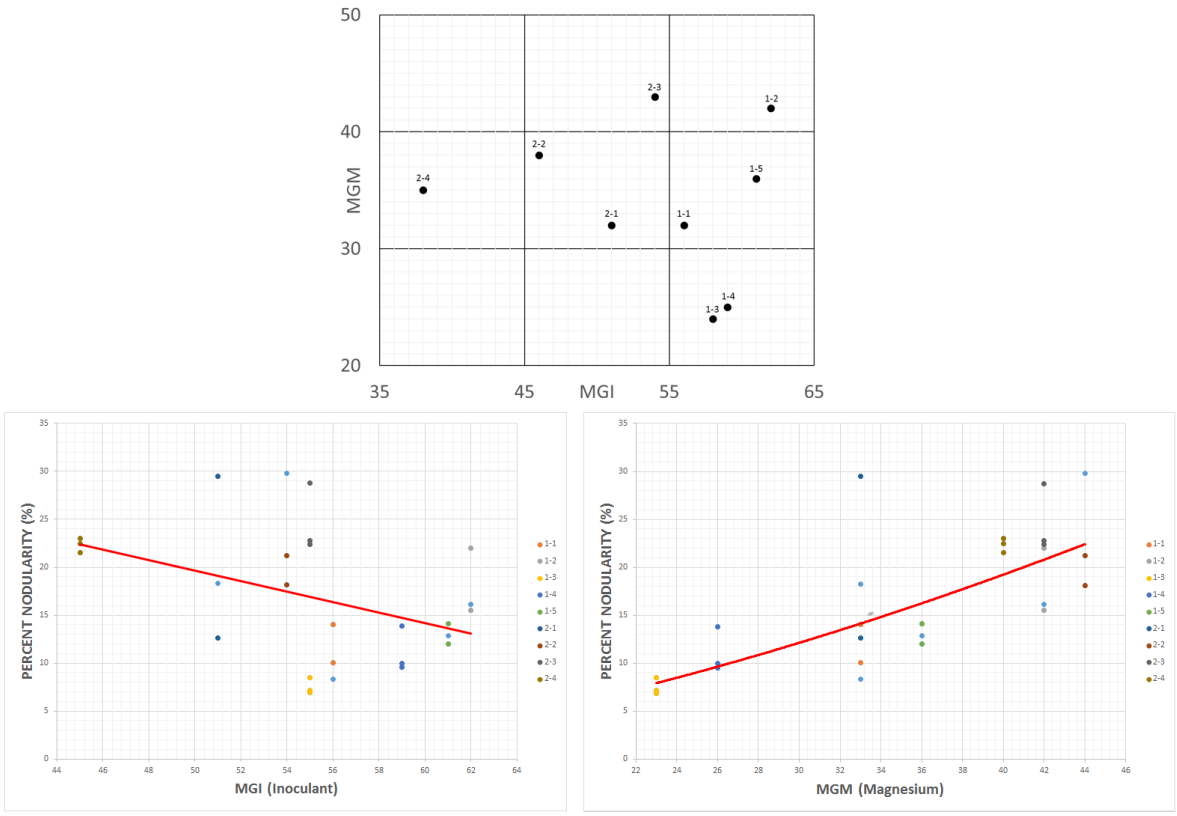

Figure 32 - Comparison between both Mg and Inoculant additions in each sample and the respective percentage of nodularity.

Despite the fact that both graphs show a approximated linear relation, the conclusions expressed above are not very accurate, since the nodularity values obtained are too disperse.

Nonetheless, what is clear is that all samples except one with levels of nodularity above 15% expressed some kind of porosity. Likewise, all samples except for one with a low percentage of nodularity – under 12% – showed no sign of porosity in them.

With that said, it could be concluded that high nodularity leads to the presence of porosity.

10.4 SEM and EDS ANALYSIS

The images of the surface of the pores obtained with SEM reveal clear differences in the morphology of the porosity.

The gas pores, bigger in size and with a smoother uniform surface, are easily distinguishable from the shrinkage pores that are smaller and have an irregular surface. The SEM images show that within the shrinkage porosity there are two other separate kinds of pores that also differ from each other.

One type of pores has a regular dendritic shaped surface, where the dendrites contain both primary and secondary arms; whereas the surface of the other type of pores lacked the secondary arms growing from the main primary dendritic arms.

The discrepancy in this two shapes is supposedly due to the fact that the pores were formed during separate stages of solidification. This means that the pores containing the regular shaped dendrites were formed earlier than the ones with the dendrites missing the secondary arms. Figure 33 describes in what phases of the solidification process the different types of porosity are meant to be formed.

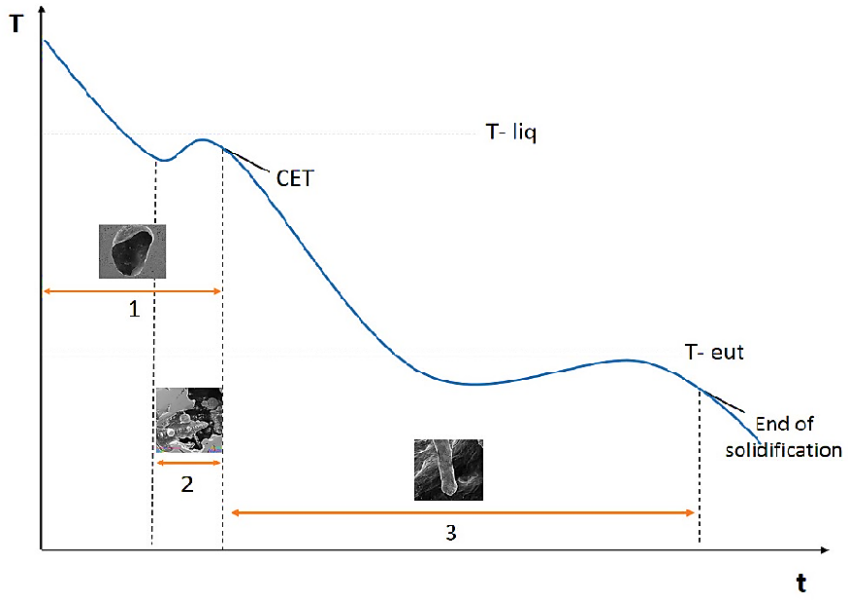

Figure 33 - Schematic diagram of a CGI cooling curve, demonstrating the time chronology of the formation of different pores. 1 - Gas Pores; 2- Shrinkage Pores with Regular Dendritic Shape; 3 - Shrinkage Pores with Irregular Shape missing Secondary Arms [9].

It is suggested that the irregular dendrites, lacking the secondary arms, were in contact with the melt for a longer period of time. What happens is that the secondary arms tend to be remelted in the liquid after their formation, while they were still in contact with it. This then leads to the continuous loss of the secondary arms, until the dendrites are entrapped in the pores and there is no longer any contact with the melt.

As for the surface of the gas pores, there were no dendrites appearing from the SEM analysis. A clear comparison between the three types of pores is shown in figure 34. Also, the figure shows in what samples the separate kinds of porosity are presented. There is no clear relationship between what type of porosity tends to be formed and the amounts of Mg and Inoculation in each sample.

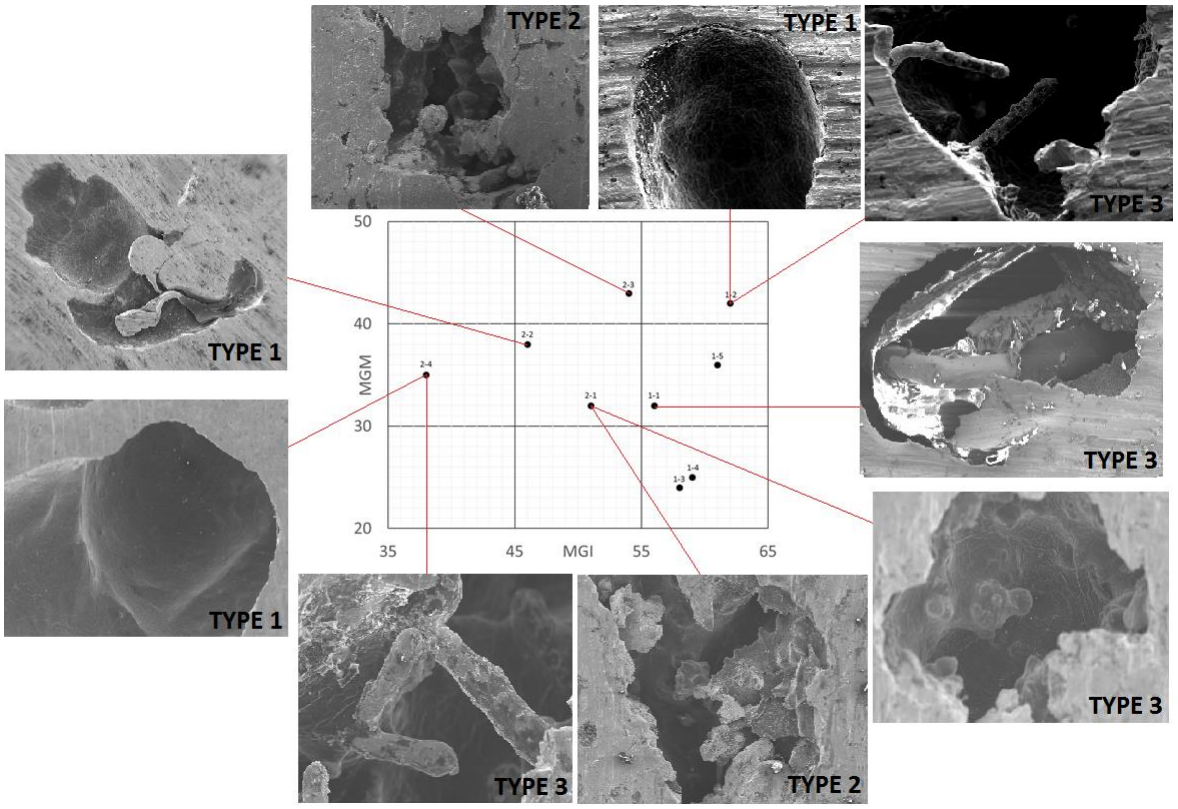

Figure 34 – Different types of porosity present in the CGI samples.

When it comes to the EDS analysis, the goal was to study the composition of the surface of the pores. As it has been previously reported by several experimental works, it is a common feature of cast iron porosity to have a graphite layer being formed on the surface of the pores. The formation of this carbon layer is driven by carbon diffusion through the material towards the surface of the pores [26, 27].

It is also claimed that if the layer has a continuous shape, meaning it uniformly covers the surface, the main gas connected to that specific porosity is meant to be hydrogen. On the other hand, if that carbon layer is not uniform and continuous, the gas associated with that porosity would be nitrogen [9].

As it is seen in figure 35, the morphology of the surface of the pores varies between different samples. The picture on the right shows a dendrite that is covered by a uniform carbon film, with an area on the left where it got removed, possibly due to the cutting process. Whereas on the other picture, it is visible that the dendrites have an irregular shaped surface, with the carbon film being only deposited in some areas.

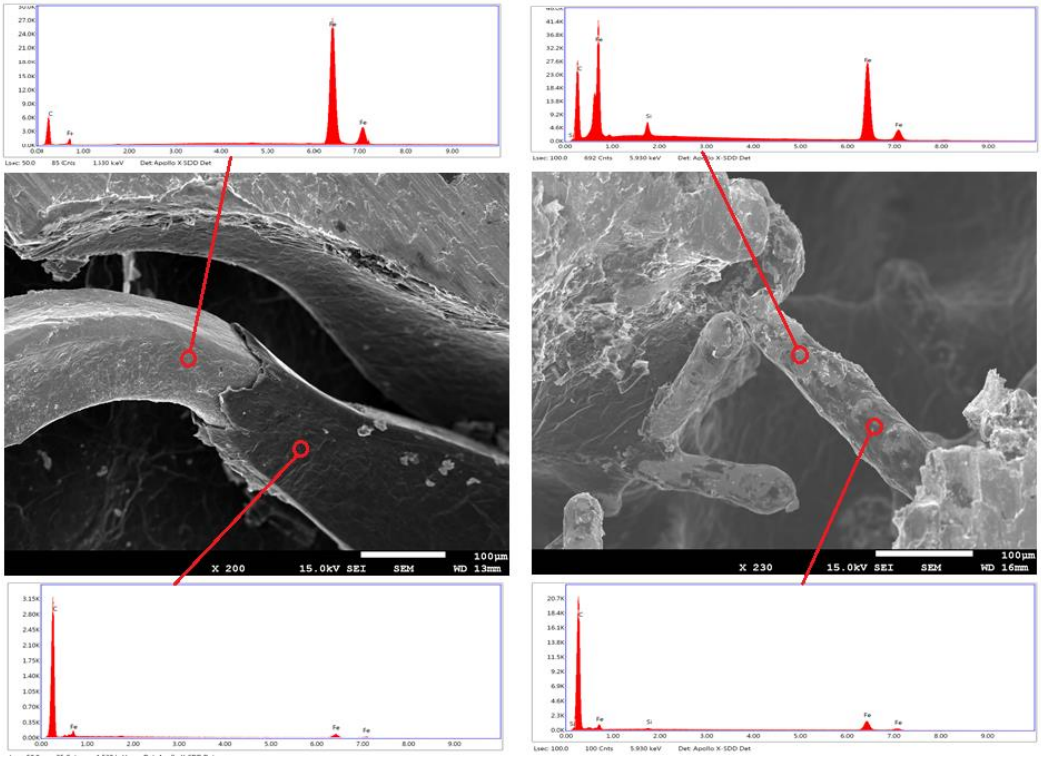

Figure 35 – Information obtained from the EDS analysis of the surface composition inside two shrinkage pores.

This discrepancy in the homogeneity of the layers goes to show that the porosity might be connected to different gaseous elements for different samples.

An observation of the bigger gas pores showed that their surfaces were covered with a uniform carbon film throughout the whole pore.

None of the pores were covered by an oxidized surface, which proves that in no sample the porosity was in contact with the atmosphere at high temperatures [9].

CHAPTER 4

This chapter displays the most significant remarks obtained from this study, as well as some suggestions for future work that could be interesting and valuable to carry on.

11 SUMMARY OF RESULTS AND CONCLUSIONS

The following remarks are based on results from the different tests and measurements conducted throughout this study, and are briefly summarized:

- The ultrasound analyses demonstrated that the identification of porosity with the use of a simple portable equipment is not ideal – not leading to optimal results, although a decent evaluation was achieved.
  A better solution could obviously be the use of more advanced devices, that are not as dependent on the user's judgement, based purely on signal discrepancy, for the prediction of porosity.

- By characterizing the graphite in all samples, it can be concluded that there is a tendency for the appearance of macro porosity (gas pores) in cases of higher nodularity. The amount of porosity is also increased for higher number of graphite nodules in the microstructure.
  The relationship between the parameters of added Mg and Inoculant and the level and type of porosity is unclear.

- The Color Etching revealed the CGI microstructure that included some graphite nodules enveloped in the dendrites (primary austenite). Also, the nucleated eutectic colonies (secondary austenite), with vermicular graphite being formed within them, were shown to be in contact with the austenite dendrites.

In terms of the graphite nodules, two different types of spheroidal graphite were easily distinguishable. They showed different sizes and were located in separate areas with different Si segregation patterns. This gave information about the mechanisms behind their nucleation and when during the solidification process they were formed.

- The results obtained from SEM showed that three different types of porosity for separate cases. There was a clear difference between the internal surface of the gas pores and the other two types of what was characterized as shrinkage pores.
  Most of the shrinkage porosity was found in the last solidified regions. The pores that were supposedly formed in later stages of solidification had irregular shaped dendrites inside them missing secondary arms.

- The EDS analysis allowed the identification of a carbon layer that covered the surface of the pores. This thin film was formed uniformly on top of some of the pores, while it had an irregular shape in other cases. This difference could be linked to difference gaseous sources.

12 FUTURE WORK

Due to the fact that this study was limited in time to a just few months, there was a relatively shortage in results. Some other experimental approaches could be carried over, in order to achieve better conclusions.

Although this work was all based on samples with the same size and geometry, two other types of components are available for analysis. They were casted with the same shape and geometry, but differ in size – one set of samples has a higher diameter and the other set is smaller.
Their porosity study and characterization would be of most interest in order to possibly drive better and more congruent conclusions, when it comes to the correlation with the parameters of added Mg and Inoculant.

AKNOWLEDGEMENTS

I would like to take this chance to express my gratitude to:

Professor **Attila Diószegi**, for his professional guidance and for providing me with the opportunity of being a part of this project.

Professor **Carlos Silva Ribeiro**, for everything that he has taught me.

Lucian Vasile Diaconu, for his supervision, his support and help throughout the whole project.

Björn Domeij, for the constant positive attitude, for always being available to help me and for guiding me in the right direction.

Zoltan Diószegi for his assistance and welcoming reception at Volvo SA.

Jörgen Bloom for all the help and teachings using the various experimental equipments.

All members of the Department of Materials Science at Jönköping University who were always so kind and friendly.

And finally, to my parents for being so caring and supportive.

Francisco Fonseca

Jönkoping, 2017

REFERENCES

1. Siafakas, D., *Investigation of Hydrogen and Nitrogen Content in Compacted Graphite Iron Production*. 2013.
2. Dawson, S. and F. Hang, *Compacted graphite iron-a material solution for modern diesel engine cylinder blocks and heads*. China foundry, 2009. **6**(3): p. 241-246.
3. Dawson, S. *Process control for the production of compacted graphite iron*. in *106th AFS Casting Congress, Kansas City*. 2002.
4. López, M., et al., *Solidification Macrostructure of Compacted Graphite Cast Iron and its relationship with Shrinkage Porosity*. 2014.
5. Vazehrad, S., J. Elfsberg, and A. Diószegi. *On factors influencing macro shrinkage porosity formation in compacted graphite iron*. in *Materials Science Forum*. 2014. Trans Tech Publ.
6. Guesser, W.L., P. Duran, and W. Krause, *Compacted graphite iron for diesel engine cylinder blocks*. Congrès Le diesel: aujourd'hui et demain Ecole centrale, 2004: p. 1213.
7. Dawson, S. and T. Schroeder, *Practical applications for compacted graphite iron*. AFS Transactions, 2004. **47**(5): p. 1-9.
8. König, M., *Microstructure formation during solidification and solid state transformation in compacted graphite iron*. 2011.
9. Vazehrad, S., *Shrinkage Porosity Characterization in Compacted Cast Iron Components*. 2012.
10. Stefanescu, D.M., R. Hummer, and E. Nechtelberger, *Compacted graphite iron*. ASM International, Metals Handbook. Tenth Edition., 1990. **1**: p. 56-70.
11. Goodrich, G.M., *Introduction to Cast Irons*, in *ASM Handbook*. 2008, ASM International. P. 785-811.
12. Campbell, John. "A hypothesis for cast iron microstructures." *Metallurgical and Materials Transactions B* 40.6 (2009): 786-801.
13. Skaland, T., Ø. Grong, and T. Grong. "A model for the graphite formation in." *Metallurgical and Materials Transactions A* 24.10 (1993): 2321-2345.
14. Stefanescu, D., *Science and engineering of casting solidification*. 2015: Springer.
15. Stefanescu, D., et al., *Particle Engulfment and Pushing By Solidifying Interfaces-Recent Theoretical and Experimental Developments*. 2003.
16. Sigworth, G., et al., *Porosity formation in modified and unmodified aluminum±silicon alloy castings*. AFS Trans, 1995. **102**: p. 245-261.
17. Lee, S.-C. and J.-M. Suen, *Ultrasonic nondestructive evaluation of matrix structures and nodularity in cast irons*. Metallurgical transactions A, 1989. **20**(11): p. 2399-2407.
18. Orłowicz, W., et al., *Evaluation of ductile iron casting material quality using ultrasonic testing*. Journal of Materials Processing Technology, 2010. **210**(11): p. 1493-1500.
19. Krautkrämer, J., *Determination of the size of defects by the ultrasonic impulse echo method*. British Journal of Applied Physics, 1959. **10**(6): p. 240.
20. Krautkrämer, J. and H. Krautkrämer, *Ultrasonic testing of materials*. 2013: Springer Science & Business Media.
21. McMaster, R.C., *Nondestructive testing handbook. Volume 1-Leak testing*. 1982.

22. J. Zhou, F. Zhong, W. Schmitz, S. Engler, Application of a new color metallography technique to cast iron, Prakt. Metallogr. 30 (3) (Mar. 1993) 122–128.
23. E. Beraha, B. Shpigler, Color Metallography, 1st ed. ASM, Metals Park, Ohio, 1977.
24. F. Chen and J. Keverian, “Effect of nitrogen on subsurface pinholes in steel castings”, Modern Casting, Vol. 50, No.1, pp. 95-103, (1966).
25. E. Weck, E. Leistner, Metallographic Instructions for Color Etching by Immersion, Part I: Klemm Color Etching, 1995.
26. J. M. Greenhill, Diagnosis of Causes of Defects, Foundry Trade Journal, Vol. 129, no. 2812, pp. 603-608, 29 Oct, (1970).
27. C.W.Jr. McCauley and T.S. Sadarshan, Subsurface Defects in Cast Irons, Metallugraphy, Vol. 12, No. 4, pp. 325-332, (1979).
28. König, Mathias. *Microstructure formation during solidification and solid state transformation in compacted graphite iron*. Diss. Chalmers University of Technology, 2011
29. Standard, I. S. O. "16112 (2006)‘Compacted (vermicular) graphite cast irons–classifications’." *International Organization for Standardization, Geneva, Switzerland*.